https://doi.org/10.5194/egusphere-2026-1505
Preprint. Discussion started: 26 March 2026

Tracking sulfate, magnesium, phosphorus and amorphous phases in Rosalina-like benthic foraminifera

Guillaume Paris[1], Caroline Thaler[2,3,*], Marc Dellinger[4], Jérôme Aléon[5], Smail Mostefaoui[5], Alice Aléon-Toppani[6], Claire Rollion-Bard[3], David Troadec[7], Guillaume Yangshu Wang[8], Annachiara Bartolini[2]

[1] Université de Lorraine, CNRS, CRPG, F-54000 Nancy, France

[2] Centre de Recherche en Paléontologie -Paris (CR2P), MNHN, CNRS, Sorbonne Université, F-75005 Paris, France

[3] Laboratoire des Sciences du Climat et de l'Environnement (LSCE), UMR 8212 CEA, CNRS, Université de Versailles Saint-Quentin en Yvelines, F-91191 Gif sur Yvette Cedex

[4] MCAM, UMR 7245 MNHN, CNRS, Sorbonne Université, 75005 Paris, France

[5] Institut de Minéralogie, de Physique des Matériaux et de Cosmochimie (IMPMC), Sorbonne Université, MNHN, CNRS UMR 7590, IRD, F-75005 Paris, France

[6] Université Paris-Saclay, CNRS, Institut d'Astrophysique Spatiale, F-91405 Orsay, France

[7] University Lille, CNRS, Centrale Lille, Junia, University Polytechnique Hauts de France, UMR 8520-IEMN, F-59000 Lille, France

[8]Université Paris Cité, Laboratoire Matériaux et Phénomènes Quantiques UMR 7162, 75205 Paris, France

* now at Ecobloom

Correspondence to: Guillaume Paris (guillaume.paris@univ-lorraine.fr)

Abstract

In this study, we combined high resolution Transmission Electron Microscopy (TEM) bright field and High-Angle Annular Dark-Field Scanning TEM imaging with nanoscale Secondary Ion Mass Spectrometry (NanoSIMS) analyses of *Rosalina* like foraminifera cells cultured in ^{33}S-labeled seawater to understand the origin of sulfur in the test and the cytoplasm, its interaction with the ultrastructure of the test and the co-distribution of sulfur with phosphorus, calcium and magnesium. Test chambers that grew in ^{33}S-labeled seawater revealed that at least 1/3 of the sulfur incorporated is directly taken from seawater sulfate. Our observations reveal a global co-occurrence of P, S and Mg within the previous two last chambers of the test, that all appear more concentrated in two areas, mostly near the Primary Organic sheet (POS) and in the Outer Calcitic Layer (OCL) that corresponds to the calcite added during the growth of the last chamber. Less crystalline grains can be found in the P, Mg and S-richest part of the POS and within OCLs. We interpret these grains as ACC (Amorphous Calcium Carbonate), in association with organic matter and possibly ACP (Amorphous Calcium Phosphate) likely formed or assembled at the sites of calcification, revealing a complex interplay between S, Mg and P. This interplay could indicate an inorganic cause for S and P enrichments,

https://doi.org/10.5194/egusphere-2026-1505
Preprint. Discussion started: 26 March 2026

co-occuring with Mg enrichments and amorphous phases. Finally, ~0.1 to ~3 µm Ca-rich grains are detected in the cytoplasm. The biggest ones can be interpreted as ACC vesicles, the smaller ones are Ca and P rich and can be interpreted as autophagosomes or acidocalcisomes, the latter also containing labeled sulfur. Labeled sulfur is also found within smaller vesicles in the cytoplasm and represents overall 10 to 25 % of the sulfur we observe. Though we cannot confirm the occurrence of an assimilatory pathway for sulfur in foraminifera, the clear presence of seawater sulfate in the cell demonstrates that sulfate is involved in many aspects of foraminifera biological activity, in close association with Ca-transportation, Mg and P distribution, and likely with ACC formation and its evolution to calcite.

1. Introduction

Sulfate is the second most abundant anion in the modern ocean, (~28 mmol L^{-1}), though its concentration fluctuated massively over Earth's history (e.g. Timofeeff et al., 2001; Horita et al., 2002; Crowe et al., 2014; Fakhraee et al., 2018; LaFlamme et al., 2021). Sulfur has four stable isotopes (^{32}S, ^{33}S, ^{34}S and ^{36}S) and the sulfur isotopic ratio of the most abundant isotopes is homogeneous in the modern ocean ($\delta^{34}S_{sw}\approx21‰$) (Craddock et al., 2008; Paris et al., 2013; Rees et al., 1978; Tostevin et al., 2014), where $\delta^{34}S=[(^{34}R_{sample}/^{34}R_{VCDT})-1]$ with $^{34}R=^{34}S/^{32}S$ and VCDT (Vienna Canyon Diablo Troilite) is the international standard (Coplen and Krouse, 1998). Sulfate (SO_4^{2-}) plays a major role in anoxic sediments, where microbial sulfate reduction (MSR) is the most important anaerobic pathway through which organic matter is remineralized (Berner and Canfield, 1989; Canfield and Raiswell, 1999; Claypool et al., 1980; Paytan et al., 1998; Present et al., 2020; Rennie et al., 2018). As a result, variations of $\delta^{34}S_{sw}$ over time can help to constrain changes in the sulfur cycle and its links with the carbon and oxygen cycles. Among the available proxies to reconstruct $\delta^{34}S_{sw}$, Carbonate Associated Sulfate (CAS) has become an increasingly popular archive to investigate the Phanerozoic and the Precambrian (e.g. Burdett et al., 1989; Ohkouchi et al., 1999; Kah et al., 2004; Osburn et al., 2015; Gomes et al., 2016; Present et al., 2020), and even the Archean (Paris et al., 2014b, 2020).

The use of sulfur isotope ratios measured in CAS extracted from biogenic carbonates has sparked the debate of the nature of the phase bearing sulfur in biogenic calcite (e.g. Cuif et al., 2003; Dauphin et al., 2003, 2005, 2013; Cusack et al., 2008; Richardson et al., 2019b). CAS is sulfate inorganically incorporated within the crystal lattice of calcium carbonates (Fernández-Díaz et al., 2010; Kampschulte et al., 2001; Paris et al., 2014a). Over the last decades, sulfur isotopes of CAS from inorganic and most biogenic carbonates have been shown to display small fractionations (-1 to +4 ‰) from the fluid from which they grew, whether in biogenic or inorganic carbonates (Barkan et al., 2020; Bryant et al., 2023; Paris et al., 2014a; Rennie et al., 2018; Thaler et al., 2023), though small scale variability (≈ 1-3 ‰) can be found, in brachiopods shells or coral skeletons (He et al., 2024; Present et al., 2015). However, sulfur is common in organic matter as well (Oae, 2012), and, in biocalcifying rotaliid foraminifera, its global isotopic signature is distinct from that of the sulfate directly incorporated into calcite (e.g. Thaler et al., 2023). Knowing sulfur location, speciation and origin is indeed important to better understand the CAS archive, including CAS from calcitic foraminifera tests, that are one of the most used archive for reconstructions of paleoenvironmental conditions (e.g. Rennie et al., 2018; The Cenozoic CO2 Proxy Integration Project (CenCO2PIP)

Consortium et al., 2023). In addition, sulfur speciation may impact how the original signal is preserved during diagenesis (Richardson et al., 2021).

More generally, sulfate is a critical anion in biogenic calcite formation for three reasons. First, sulfate plays a role in the precipitation of calcite vs. aragonite (Bots et al; 2011, Barkan et al., 2020): at high sulfate concentrations, such as in modern seawater, calcite precipitation is inhibited. Second, the physiological activity of foraminifera requires sulfate, as shown by the death of benthic foraminifera cultivated in sulfate-free or -poor artificial seawater (Thaler et al. 2023). This is coherent with the need for sulfur in organic matter, but other reasons could explain the need for sulfate, such as sulfate assimilation. In eukaryotes, the presence of sulfate reduction pathway is assumed to be restricted photosynthetic cells (Patron et al., 2008; Schiff, 1980). Nonetheless, culture experiments using ^{34}S-enriched seawater sulfate produced labeled sulfur enrichments within chloroplasts taken from algae (kleptoplasts) or endosymbiotic prokaryotes. Such enrichments have been interpreted as the result of intracellular assimilatory sulfate reduction (Jauffrais et al., 2019; LeKieffre et al., 2022; Nomaki et al., 2016). Thus, reduced sulfur could be provided by food or through seawater sulfate reduction. Third, sulfur also occurs as sulfate in organic matter in the test. Sulfate enriched glycosaminoglycans, which are complex polysaccharide molecules constituted of a sequence of amino sugars that are covalently attached to proteins, are thought to act as a template for biomineralization (Angell, 1967; Bé et al., 1979; Dauphin et al., 2008; Falini et al., 1996; Hemleben et al., 1986; Langer, 1992; Spero, 1998; Weiner and Erez, 1984). For instance, coral cells produce an extracellular matrix on which calcium carbonate precipitated because negatively charged groups able to bind calcium are regularly spaced and act as template on which $CaCO_3$ nucleates and precipitates (Addadi et al., 1987; Falini et al., 2015; Helman et al., 2008; Tambutté et al., 2007).

Such processes may occur also in Rotaliida, which is the most diversified order of biocalcifying foraminifera in the ocean and includes both benthic and planktic species. The distribution of sulfur in their tests, like many other elements such as P and Mg, is characterized by well-documented banding structures at the micron or sub-micron scales, (van Dijk et al., 2019a; Eggins et al., 2004; Fehrenbacher et al., 2017; Geerken et al., 2019; Glock et al., 2019; Lemelle et al., 2020; Paris et al., 2014a). In rotalid foraminifera, banding appears to be linked to the multi-layered growth of the test, which is characterized by the sequential addition of chambers. The initial stage is the formation of a precursor layer, which is proposed to act as an organic template and has been named primary organic membrane, sheet or zone (POM, POS or POZ Hemleben et al., 1977, 1986; Bé et al., 1979; Erez, 2003; de Nooijer et al., 2014; Lemelle et al., 2020; Tyszka et al., 2021). The subsequent stage of the wall growth is a bi-directional precipitation of two calcite layers on both side of the POS. The inner calcitic layer (ICL) is precipitated between the inner organic layer (IOL) and the POS, while the outer calcitic layer (OCL) is precipitated between the POS and the outer organic layer (OOL). In the end, the multi-layer nature of the wall results from the successive additions of new chambers, with a new OCL covering the entire test each time that a new chamber is added. Yet the meaning of this banding depends on the elements investigated.

On the one hand, sulfur and magnesium (co-)bandings have been found in rotaliid foraminifera and other organisms, and magnesium is usually interpreted as associated to the inorganic calcium carbonate phase of the test rather than to organic matter (van Dijk et al., 2017; Lorens and Bender, 1980; Paris et al., 2014a; Richardson et al., 2019a; Spero et al., 2015a; Tanaka et al., 2019). Accordingly, Mg has been shown to be solely inorganically substituted for Ca within the calcite mineral lattice, despite changes in Mg/Ca ratio (Branson et al., 2013). On the other hand, shared S and P banding has also been documented and interpreted as reflecting variations in organic matter (OM) within the test (e.g., Glock et al., 2019; Geerken et al., 2019). Thus, sulfur would reveal the organic linings, consistent with the presence of organically bound sulfate within the organic matter in the test, as well as S-containing amino acids (Dauphin et al., 2013; Richardson et al., 2019b) and the role of sulfated molecules in biomineralization.

However, this classical view (P and S track organic matter, Mg variations are purely inorganic) has been challenged over the years. Sulfate, like Mg, is inorganically incorporated in calcite (Busenberg and Plummer, 1985; Kontrec et al., 2004), though high concentration of sulfate – similarly to Mg – inhibits calcite and favors aragonite precipitation (Barkan et al., 2020; Bots et al., 2011). Even though the need for low sulfate could suggest that foraminifera would try to exclude sulfate from the site of biomineralization, the occurrence of inorganic sulfate in biogenic calcite implies that sulfate is still present in the calcifying fluid (van Dijk et al., 2017; Erez, 2003; Paris et al., 2014a; Richardson et al., 2019a; Thaler et al., 2023). Phosphate also is inorganically included in calcite lattice. Even at low phosphate concentrations (few tens of µmol L^{-1}), inorganic experiments show that phosphate can be adsorbed on the surface of the mineral, incorporated into the growing crystal, or precipitated as calcium-phosphate (House and Donaldson, 1986; Plant and House, 2002; Ren et al., 2021). In addition, phosphate ions are also known to inhibit calcite formation (Burton and Walter, 1990; House, 1987; Lin and Singer, 2006), they share thus one more point with magnesium and sulfate. Mg, S and P can all be inorganically included in calcium carbonate. Finally, enrichment of Mg (and Na) in the POS of *Orbulina universa* has been interpreted as a contribution of organically-carried Mg (Branson et al., 2016), showing that Mg might not be purely inorganically present in the test, suggesting that all three elements can also be associated to another phase than calcite.

In this regard, we try to understand the trajectory of sulfur from seawater sulfate to its incorporation into calcite, as well as the co-distribution of S, P ang Mg and the combined roles of those elements in the structuration of the test. The hypothesis is that inorganic sulfate in the test (CAS) as well as the sulfate groups associated with organic molecules come directly from seawater, in which case they could be expected to both have similar isotopic ratios. By contrast, whether it comes directly from food or through assimilatory sulfate reduction if it occurs in the cell, reduced sulfur in organic matter is most likely isotopically different.

To achieve this, we cultivated rotaliid benthic foraminifer *Rosalina*-like in artificial seawater in different conditions, including seawater enriched in the rare sulfur isotope ^{33}S or seawater with natural isotope abundances but feeding the foraminifera using ^{33}S-enriched algae. We applied a new protocol for chemically fixing the foraminifera in order to preserve simultaneously the cytoplasm and the test. We then used NanoSIMS (Nanoscale Secondary Ion Mass Spectrometer) to image the distribution of sulfur isotopes in the cell and the growing structure of the foraminiferal test wall at the nanoscale, as well as P and Mg distribution. Combined with high resolution Transmission Electronic Microscopy (TEM) bright field and Scanning Transmission Electronic Microscopy (STEM) high-angle annular dark-field (HAADF) imaging of Focused Ion Beam (FIB) produced lamellas, this strategy illuminated the sites within cytoplasm and the test where sulfur was preferentially incorporated from seawater and its association to Mg and P distribution.

2. Material and methods

2.1 Foraminiferal strain

Benthic foraminifera were grown at the free living protist collection facility (collection group: Biological Resources of Living and Cryopreserved Cells; Collection of Unicellular Eukaryotes) at the MNHN (Muséum national d'Histoire naturelle, Paris, France). We used the rotaliid benthic foraminifer strain For1C1 (MNHN-CEU-2016-0075, *Rosalina* like), initially isolated from the top layer of sediments collected off Banyuls (Mediterranean French coast) in 2006 and adapted to *in vitro* cell culture. The foraminifera are maintained through asexual reproduction in 90 mm-diameter Petri dishes in natural sea water (NSW) and fed with *Chlorogonium sp.* (strain MNHN-CEU-2016-0001), a freshwater microalga. We grew the algae under medium light intensity at 25°C in Basal Bold medium. They were then suspended in 0.22 µm filtered pH 8.2 NSW after 3 steps of rinsing with NSW. The cultures for this study were performed similarly to the cultures described by Thaler et al. (2023). The NSW was stored in a cold room at least for a month and was then filtered through 0.22 µm filters. The pH (NBS scale) was adjusted to 8.2 through addition of NaOH and/or HCl, before use. Petri dishes were maintained at 22°C using a Memmert IPP 110 plus incubator equipped with cold white light modules (5,500 K). The light followed a 12h day-12h night schedule. Foraminifera were wed with *Chlorogonium sp.* and culture water was changed once a week. The $^{34}S/^{32}S$ sulfur isotope ratios artificial seawater sulfate has been measured at $\delta^{34}S_{ASW} = 0.1 \pm 0.2$ ‰ (Thaler et al., 2023). Though not explicitly measured, we estimate that $\delta^{33}S_{ASW} \approx 0 \pm 0.2$ ‰ because ASW most likely follows ^{33}S natural abundance.

2.2 Culture in artificial seawater and ^{33}S labeling

Some individuals of the foraminiferal strain For1C1 were transferred to 0.22 µm filtered artificial seawater (ASW) prepared following Kester et al. (1967). ASW has a total salinity of 35.06 g L^{-1}, and the concentrations of the main ions are as follows (in mmol L^{-1}): Cl^- 543.9, Na^+ 467.3, SO_4^{2-} 28.2, Mg^{2+} 53.1, Ca^{2+} 9.9, K^+ 10.0, HCO_3^- 2.3, Br^- 0.8, H_3BO_3 0.4, Sr^{2+} 0.1, F^- 0.1. ASW was then left to equilibrate with the atmosphere for 2 to 3 hours and the pH was adjusted to 8.2 using NaOH and HCl. Different experiments were carried out in which the specimens were cultured in enriched ^{33}S-ASW solutions containing either the natural average ocean sulfate concentration (28.16 mmol L^{-1}) or a double sulfate concentration (56.36 mmol L^{-1}). The foraminifera were left in the ASW enriched in ^{33}S for different durations (see Table 1). Specimen Fa5B was grown in ASW without labeled sulfur but fed with algae that were grown in ^{33}S enriched solution, then abundantly rinsed to avoid transferring free $^{33}SO_4$ to the growth medium of the foraminifer. Samples were then cultured for 2 to 5 days in ^{33}S-ASW seawater with a total sulfate concentration of 28.16 mmol L^{-1}, including 1.41 mmol L^{-1} of $Na^{33}SO_4$, which results in a $\delta^{33}S$ of the culture media of approximately 7030 ‰.

Table 1 Description of the different experiments/specimens analyzed by NanoSIMS.

Strain	Specimen	Sample	Sulfate (mmol L^{-1})	Duration of experiment	Fixed specimen	chamber analyzed
Rosalina like Banyuls (For1C1)	A1	A1n-1	28.16	2 days	no	n-1
	A1	A1n	28.16	5 days	no	n
	F5(2)B	F5(2)B1	56.36	5 days	yes	n-1
	F5(2)B	F5(2)B3	56.36	5 days	yes	n-3+n-5/6
	F2A2	F2A2 n	28.16	2 days	yes	n
	Fa5B	Fa5B1	28.16	5 days	yes	n-1

We selected foraminifera that were still alive at the end of the experiment, as evidenced by pseudopodial activity. Individual A1 was observed forming chambers n and n-1 in the culture medium enriched in ^{33}S. We did not observe the formation of new chambers during the experiment for the specimens F5(2)B, F2A2 and G3-Fa5B. Therefore, we cannot be sure whether any new chamber grew for these last two individuals during the labeling experiment.

2.3 Chemical cell fixation

Most protocols for chemically fixing foraminiferal cells involves dissolving their calcium carbonate shells using EDTA (Ethylenediaminetetraacetic acid; Le Kieffre et al., 2018). Here, we present a new fixation protocol that preserves both the cytoplasm and the test. Living specimens were transferred into 2 mm diameter silicon molds. Following a protocol established for marine organisms, seawater was replaced with a Sörensen-sucrose phosphate buffer solution containing 0.1 M phosphate at pH 7.5, 0.6 M sucrose, 1 mM $CaCl_2$, 2.5% glutaraldehyde and 1% formaldehyde (Kopp et al., 2015). The specimens were left to soak in this solution for 24 hours at room temperature then washed with three repeated baths of Milli-Q water, which was made basic to pH 9 with NH_4OH. This process removes all free ions and small molecules present in the cell. Cells were then dehydrated using a graded series of ethanol solutions (50%, 70%, 90% and 100%). Finally, they were embedded in Spurr epoxy resin in four successive 1-hour baths at room temperature: bath 1: 50% resin/50% pure ethanol; baths 2–4: 100% resin. The resulting molds were then placed in a vacuum oven at 60 °C overnight.

2.4 Focused Ion Beam sections

Focused ion beam (FIB) sections of thin lamellae were performed both on chemically fixed specimens (e.g., F5(2)B and F2A) and on non-chemically fixed specimens (e.g., A1, Fig. 1). FIB sections were produced using the FEI STRATA DB 235 FIB system at the Institut d'Electronique, Microélectronique et Nanotechnologie (IEMN, Lille, France).

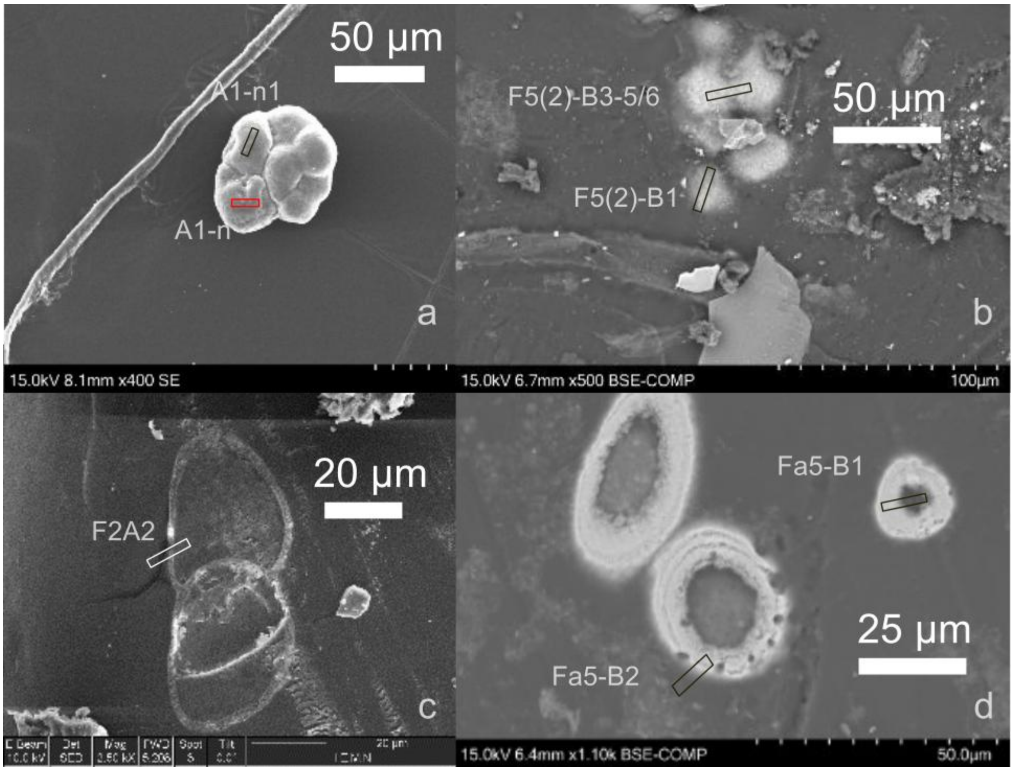

Figure 1. SEM pictures of Rosalina like benthic foraminifera, Banyuls (For1C1 strain) showing the locations of the FIB lamellas (rectangles): (a) in last (n) and penultimate (n-1) chambers of the A1 specimen (juvenile); (b) in chambers n-3, n-5/6 and n-1 of the F5(2)B specimen (adult); and (c) in chamber n of the F2A2 specimen.

We used a recently developed FIB section protocol (Aléon-Toppani et al., 2021), which enables the use of the same FIB preparation for both NanoSIMS and Transmission Electron Microscopy (TEM) analyses. Briefly, 1 µm-thick platinum (Pt) deposit was used to shield the zones of interest. A 30 kV Ga-ion beam was used to cut 1 µm-thick lamellae perpendicular to the surface of the test, revealing its growth structure and transition with the cytoplasm. The Ga-ion beam current was chosen to minimize degradation of the FIB sections. The lamellae were then extracted and sputtered damaged material was cleaned using a low-voltage, grazing-incidence Ga ion beam (5 kV). Finally, the lamellae were mounted on 1–2 µm Pt bridges, deposited in the FIB-SEM, on discoidal polished Al sample mounts that are well adapted for NanoSIMS analyses. After NanoSIMS analyses, the lamellae were recovered from the Pt bridge using the Ga beam and mounted on a TEM grid. The top surface of the FIB section was gently cleaned of NanoSIMS damage using a low-intensity Ga beam ranging from 1 nA to 300 pA. In order to enable TEM analysis, part of the lamellae that includes the entire growth structure of the wall and transition with the cytoplasm was thinned to 100 nm.

2.5 NanoSIMS analyses

NanoSIMS analyses were performed using the Cameca NanoSIMS N50 at the Institut de Minéralogie, de Physique des Matériaux et de Cosmochimie (IMPMC, Paris, France) on FIB sections mounted on Al sample mounts (see section 2.3) and coated with 20 nm gold. Analyses were performed in negative secondary ion mode using a 16 keV, Cs^+ primary ion beam of 0.5 to 1 pA, ensuring a spatial resolution of 100 to 150 nm. Using entrance and aperture slits ES3 and AS2, respectively, the mass resolving power was adjusted to ensure complete separation of polyatomic interferences, including $^{32}SH^-$ and $^{33}SH^-$ at masses 33 and 34, respectively. Phosphorus and sulfur were measured as atomic ions ($^{31}P^-$, $^{32}S^-$, $^{33}S^-$, $^{34}S^-$) and nitrogen, magnesium and calcium were measured as polyatomic ions at masses 26, 40 and 56 ($^{12}C^{14}N^-$, $^{24}Mg^{16}O^-$ and $^{40}Ca^{16}O^-$, respectively) to allow measurements at the same time as P and S isotopes. Secondary ions were collected in a combined multicollection-peak jumping mode with $^{12}C^{14}N^-$, $^{31}P^-$, $^{33}S^-$, $^{24}Mg^{16}O^-$ and $^{40}Ca^{16}O^-$ measured simultaneously on electron multipliers (EM) 1 to 5, respectively, and $^{32}S^-$ and $^{34}S^-$ measured simultaneously with EM2 and EM3 using the second magnetic field value.

To achieve sputtering equilibrium and surface cleaning before each analysis, the areas were pre-sputtered for 15 minutes with a 10 pA beam before acquisition with a raster adapted to the acquired image size. Analyses consisted in suites of 10 to 15 successive image planes with raster ranging from 7 × 7 µm to 10 × 10 µm for images of the tests and 100 to 143 image planes with raster ranging from 10 × 10 µm to 20 × 20 µm for images of both tests and fixed cells. All image planes are 256 × 256 pixels with a dwell time of 3000 µs/pixel. The total duration of individual analyses varied from ~ 47 minutes to ~ 8 hours and 6 maps were acquired on four different foraminifera specimens.

In the following, elemental results are shown as raw ratios normalized either to CaO^- or CN^-. Although the relative sensitivity factors required to determine absolute concentrations were not measured due to the lack of appropriate standards for carbonate-organic mixtures, secondary ion intensity ratios were used to account more accurately for variations of these instrumental mass biases, thus allowing the determination and study of relative variations of the intensities of Mg and S in the carbonate matrix. Secondary ion intensities are reported in total number of counts (cts) over the course of an analysis.

$^{34}S/^{32}S$ and $^{33}S/^{32}S$ ratios are presented as δ values uncorrected for instrumental mass fractionation (IMF), again due to the lack of appropriate standard for its determination of in carbonate-organic mixture. The $^{34}S/^{32}S$ ratio was used as a reference internal to each acquisition to ensure that this IMF remained negligible within uncertainty and to monitor the stability and reproducibility over the duration of the analytical session. S isotopic ratios are reported in ‰, where $\delta^{3x}S = (^{3x}S/^{32}S)_{sample}/(^{3x}S/^{32}S)_{V\text{-}CDT}-1$. V-CDT is the international Vienna Canyon Diablo Troilite standard. Because the main source of uncertainty is by far counting statistics within regions of interest (ROI) of variable sizes extracted from the images by image processing, reported errors correspond to counting statistics and are controlled by secondary ion intensities of the minor isotopes.

Images were corrected for detector dead time (44 ns) and lateral drift during analysis. Data from ROIs within images and intensity profiles were extracted from bulk images with summed individual cycle planes using the LIMAGE software (© L. Nittler).

2.6 Electron Microscope analyses

High resolution Transmission Electron Microscope (TEM) bright field and high-angle annular dark-field (HAADF) Scanning Transmission Electron Microscope (STEM) imaging of FIB lamellas were performed on a spherical aberration-corrected JEOL ARM 200 F microscope operating with a cold FEG at 200 kV at the Advanced Electron Microscopy Platform, Materials and Quantum Phenomena Laboratory (MPQ, Paris, France). For the HAADF-STEM imaging the length of the camera was of 80 mm. The TEM views were produced on the exact same section on which NanoSIMS observations were performed, following a recently developed protocol (Aléon-Toppani et al., 2021). TEM views provided here are performed with a 5° tilt. Additional views with a -5° and 0° tilt are available as supplementary figure Fig. S1.

3. Results

3.1 Electron Microscope observations of the test wall microstructure

Both bright field TEM and HAADF-STEM observations reveal the multi-layer growth microstructure of the chamber wall of a *Rosalina*-like specimens remarkably well in the FIB lamella F5(2)B1, which was cut perpendicular to the surface of chamber n-1 (Fig. 2). The dark color of the layers in the bright-field TEM image (Fig. 2a) suggests that they are crystalline because they are in diffraction position and correspond to the inner (ICL) and outer (OCL) calcitic layers. The laterally heterogeneous lightness or darkness of the grey in the outer calcitic layers is intriguing. Furthermore, the orientation of the darker and lighter grey zones changes preferentially between the two outer calcitic layers. Notably, there is a lateral alternance of white, light grey and dark grey oblique zones, especially in the main calcitic layer of the chamber (OCL_{n-1}). We count two additional OCL, one that we identify as OCLn and another, much thinner one. We interpret it as being associated to the onset of the building of a new chamber, possibly interrupted as the foraminifera was transferred to the labeled medium. This OCL will be labeled $_{n+1}$. The TEM bright field oblique white zones correspond to the darkest oblique zone in the STEM images and reveal a non-crystalline, less dense nature similar to that of the organic layers (IOL, POS, OOL).

The white zones that draw irregular lines in Figure 2a are interpreted as non-crystalline structures for three reasons. First, the portion of the FIB lamella analyzed by TEM is homogeneous in thickness, thus changes in brightness cannot be explained by a change in thickness of the sample. Second, brighter areas in bright field TEM views are explained by less dense and/or less crystalline structures. Third, changing the tilt of the section does not modify the brightness of those zones (Fig. S1), which is best interpreted as amorphous/non crystalline structures. In contrast, the dark zones show that the material is crystalline, with different orientations because the level of darkness changes with a modification of the tilt (Fig. S1). HAADF imaging supplements the information provided by TEM. The level of darkness in the image of Figure 2b can indicate the average density and chemical composition of the structures, with darker areas indicating "lighter", less dense material and lighter areas indicating denser material with a heavier chemical composition. Thus, the four almost continuous layers that appear white in the TEM bright-field view (Fig. 2a) and black in the HAADF-STEM view (Fig. 2b) are characterized by non-crystalline, less dense and chemically lighter material and likely correspond to the IOL, POS and OOL of the chamber n-1, as well as the OOL_n and OOL_{n+1}. The POS is found alongside coarse, block-like amorphous/organic phases (see Fig. 2c and d). Overall, these images clearly shows the addition of a new OCL_n, and the inner wall IOL_{n-1}-ICL_{n-1}-POS-OCL_{n-1}-OOL_{n-1}-OCL_n-OOL_n-OCL_{n+1}-OOL_{n+1} microstructure (Fig. 2a,b).

Furthermore, the shades of grey within the OCLs (darker or lighter) in bright-field TEM views mostly reflects crystal orientation within the polycrystalline structure of the test. In the STEM image (Fig. 2b), the calcitic layers appear homogeneous, indicating homogeneous density, which could support the interpretation of the bright field TEM shades as reflecting crystal orientation. At high resolution, the outer calcitic layers reveal a nanogranular structure. This structure appears darker in the STEM image (Fig. 2j) and brighter in the TEM images (Figs. 2h and 2i) than the grey background. This suggests that these "nanogranules" are less dense, chemically lighter and less crystalline than the surrounding calcite.

https://doi.org/10.5194/egusphere-2026-1505
Preprint. Discussion started: 26 March 2026

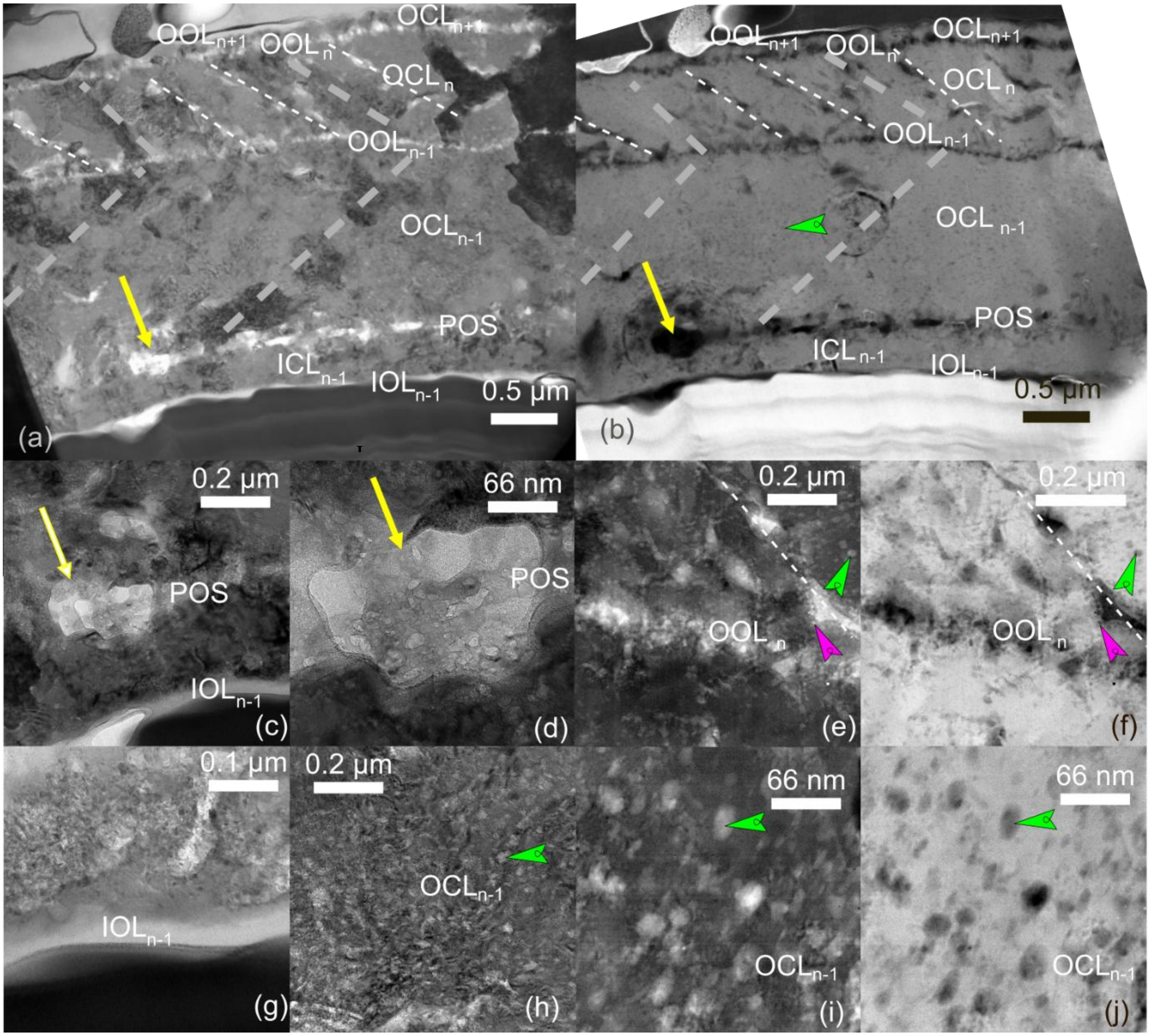

Figure 2. TEM bright field (a,c,d,e,g,h,i) and HAADF-STEM (b,f,j) images from the FIB of foraminifera (2)B1 (chamber n-1) taken after NanoSIMS analysis. (a) The global view of the FIB section shows amorphous areas (white) and crystallized zones (dark grey to darker grey) within the test. (b) In HAADF-STEM view, they correspond to less (dark) and more (grey) dense areas, respectively, with lighter (dark) and heavier (grey) chemical composition. Oblique dotted lines are additional structures found within the OCL$_n$. The very thin most external OCL is the final chamber that the foraminifera started building right before it was transferred (OCL$_{n+1}$) with the most external OOL (OOL$_{n+1}$), that is only partially preserved along the test. The white dotted lines likely correspond to amorphous-less dense oblique structures that appear similar to the different OLs, while the grey dotted line correspond to a TEM bright field structure that is not found within the HAADF image. The dense material at the base of the test (b) corresponds to the Pt deposited during the preparation of the FIB. In TEM bright field images, the IOL$_{n-1}$, POS, OOL$_{n-1}$ and OOL$_n$ are recognizable by white discontinuous layers that appear black in HAADF-STEM images. (c,d) Close up view of the POS, with a focus on the area rich in white amorphous blobs, indicated by a yellow arrow, (e,f) detail of OOL$_n$; showing the organic-less dense OOL itself, as well as the base of one of the oblique structures from within OCL$_{n-1}$ (g)close-up view of the cell-test transition highlighting the IOL; (h-j)

detail of the nanogranular structure in the calcitic layers, here OCL$_{n-1}$. Green arrowheads points towards an example of nanograin in the calcitic structure at different scales, fuchsia arrowheads points towards similar nanograins on the edge of the organic lining.

3.2 Distribution of P, Mg and S in the test

NanoSIMS maps reveal the distribution of natural and isotopically labeled sulfur, enabling us to compare the distribution of sulfur to that of organic matter, calcium carbonate, and Mg/Ca banding across the microstructure of the test's wall growth. Using Ca (^{40}Ca^{16}O) and CN (^{12}C^{14}N) maps, we are first able to distinguish the test mainly composed by calcium carbonate, thus, by definition, rich in Ca, from the cellular organic matter rich in CN (Fig. 3, supplementary figures S2 and S3). In this regard, the FIB lamella across foraminifera F5(2)B reveals the most distinct S/Ca, P/Ca and Mg/Ca distributions that follow the microstructure of the test (Figs. 3, 4). A pronounced banding is observed, characterized by thin bands with high Mg/Ca, P/Ca and S/Ca ratios in the inner and outer parts of the test, separated by a broader band characterized by lower ratios.

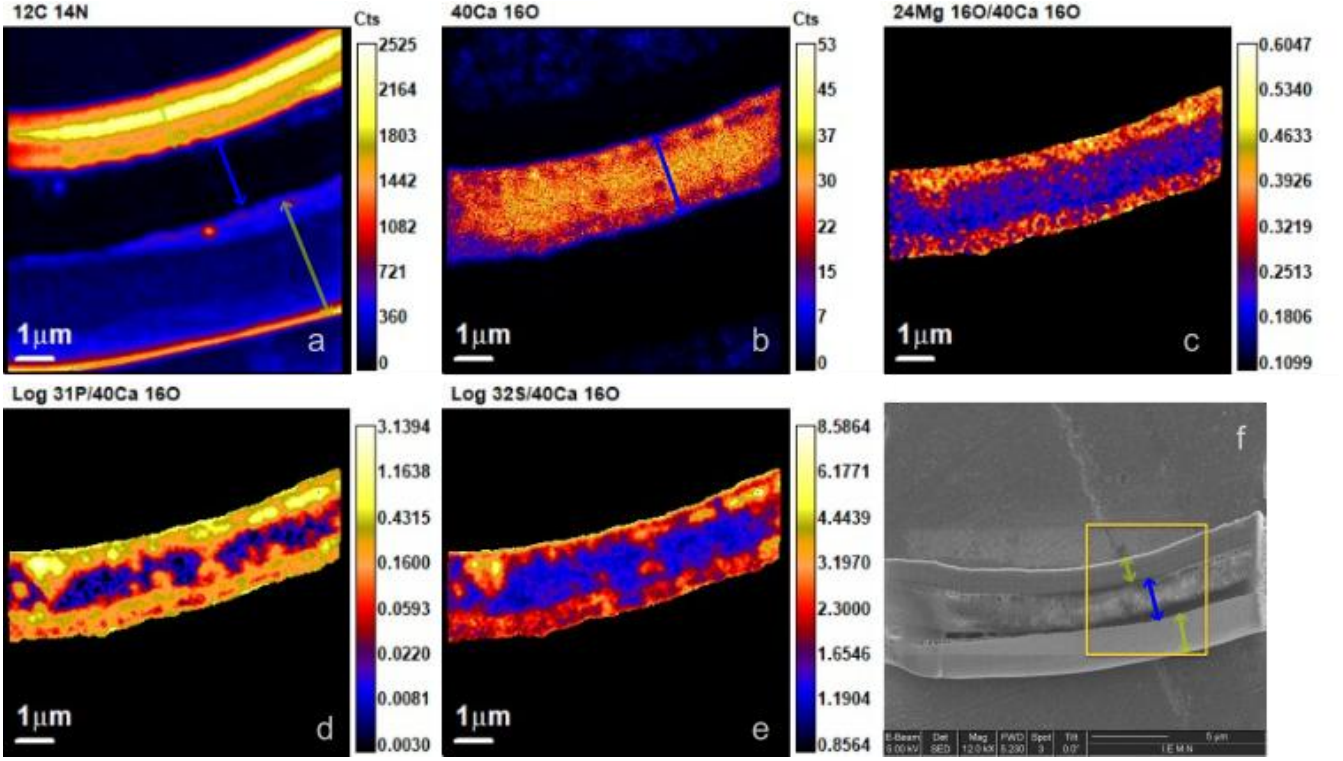

Figure 3. ^{12}C^{14}N (a), ^{40}Ca^{16}O (b), ^{24}Mg^{16}O/^{40}Ca^{16}O (c), ^{32}S/^{40}Ca^{16}O (d) and ^{31}P/^{40}Ca^{16}O (e) maps across the FIB section (f) chamber n-1 of foraminifera F5(2)B, cultured in doubled sulfate concentration seawater. The orange square in (f) indicates the location of the NanoSIMS mapping. MgO/CaO, S/CaO and P/CaO are represented only for the test. A mask was applied to avoid divergence due to the low CaO emission in the cell. Note that for P/CaO and S/CaO, the color scale is represented for the log of these ratios. Green arrows = platinum deposits; blue arrow = test.

Cross plots of element distribution within the test allow to better understand this repartition (Fig. 4, Table S1). We observe three trends in S/CaO vs. CN/CaO distribution (Fig. 4a). Trend A (red dotted line, Fig. 4) corresponds to the strongest P, S and Mg enrichments compared to CN. While S/CaO and MgO/CaO values remain higher than 1 or 0.15 cts/cts, respectively, P/CaO

https://doi.org/10.5194/egusphere-2026-1505
Preprint. Discussion started: 26 March 2026

ratios go all the way down to zero, suggesting that, unlike P, S and Mg have a background occurrence. Points defining trend A are in OCL_{n-1} and OCL_n, including OOL_{n-1} and OOL_n. Trend B (black dotted line, Fig. 4) is even more P-and S-enriched compared to Trend A, but the highest values are not systematically reached in all profiles, and this trend is most clearly visible in profiles 2 and 3, compared to profiles 1 and 4. Trend B corresponds to the enrichments of P, S and Mg across the POS. Finally, trend C (blue dotted line, Fig. 4) suggests an N-rich component where P, S and Mg remain at moderate levels. CN/CaO ratios become extremely high. However, trend C occurs only on the edges of the test (see Fig. S6 and Table S1) and could be either characteristic of IOL $_{n-1}$ and OCL_{n+1} or due to an artificial decrease of the CaO signal and increase of the CN signal as the end of the test is reached and the beam enters the CN-rich deposits. The beam size leads to an averaging across the major matrix change from calcite to cytoplasm, where S, P, Mg/Ca and Ca/CN values appear high (e.g. Fig.8). As a result, in the following, we will consider only measurements with CN/CaO values below 40, P/CaO below 1 and S/CaO below 5. Values above those thresholds are found only on the edge of the tests with the extension of trend C.

Finally, when normalized to CN and not to CaO, the covariations of S and P become obscure, and appear even anti-correlated within the points that follow trend A, suggesting that OM is not the common carrier of the two elements at least in in this trend (Fig. 4g). In addition, moderate 33S enrichments are observed, without following any clear trend.

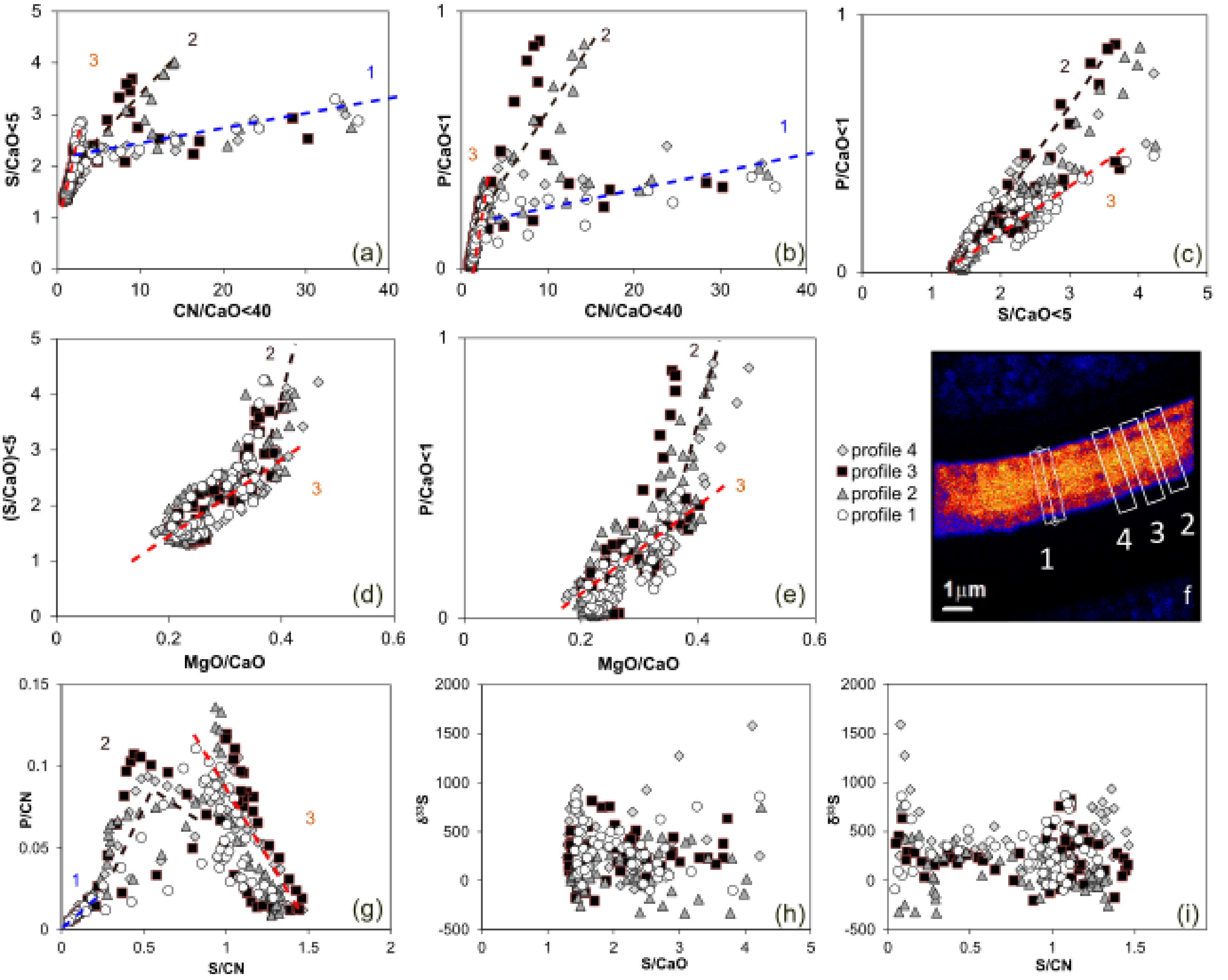

Figure 4. (a-e,g) Cross plots of elemental distribution across the test combining 4 profiles across the F5(2)B1 section, with three indicative trends. (f) Location of the four profiles selected across FIB F5(2)B1. (h,i) cross plots of $\delta^{33}S$ vs. S/CaO and S/CN data. Dotted lines are indicative, hand-drawn, trends. Only values corresponding to CN/CaO<40 cps/cps are chosen as values above this threshold correspond to the extension of trend C, likely affected by edge effects. Ratios are given in cps/cps and provide the relative distribution of elements but not absolute values.

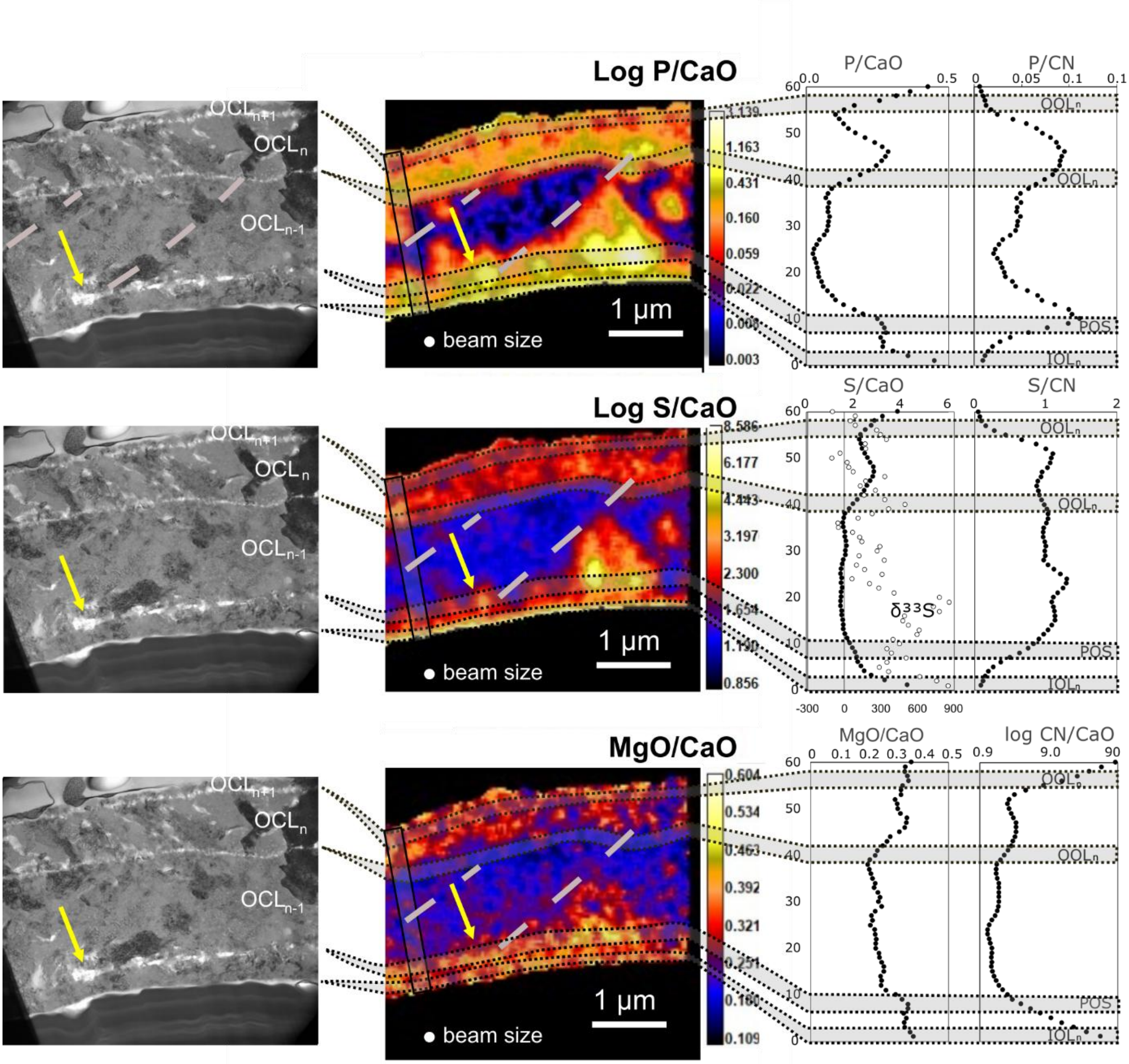

Figure 5. Combination of bright field TEM images from figure 2 with elemental maps and profiles showing the distribution of elements and elemental ratios across the wall of the chamber n-3 of foraminifera F5(2)B. The yellow arrow points to the same non crystalline blob as in figure 2. The rectangle with solid black lines indicates the location of profile 1, used to trace P/CaO, P/CN, S/CaO, S/CN, MgO/CaO and CN/CaO. The grey dotted lines indicate successions of darker TEM bright-field zones that make the transition from P, S and Mg-rich areas to P, S and Mg-poor areas.

Mg/CaO, S/CaO and P/CaO distributions across the growth structure of the wall of chamber n-1 of *Rosalina* F5(2)B are similar (Fig. 5). It should be noted first that structures smaller than the beam size (100-150 µm) cannot be distinguished and that values close to the edge are affected by the averaging across the beam surface, as mentioned previously. Overall, the outer calcitic layer deposited during the formation of the chamber selected for the FIB (OCL$_{n-1}$) has the lowest concentration in all three elements. Contrastingly, all three ratios are higher in both ICL$_{n-1}$ and the outer calcitic layer deposited while the following chamber was formed by the foraminifera (OCL$_n$). NanoSIMS resolution does not allow us to investigate the composition of OCL$_{n+1}$ whose width is about the same as the beam size.

Phosphorus reveals four enriched bands. Both P/CaO and P/CN ratios indicate the same pattern and allows to track the POS zone, as well as OCL$_n$, both enriched in this element. Both edges however, including the IOL and the OOL$_{n+1}$, appear excessively high in P/CaO and low in P/CN, which could be due to edge effect related to the beam size. As marked by the yellow arrows in figures 2 and 5, within the POS, and all the way inside the wall, the less crystalline areas are associated with the highest concentrations in phosphorus. The dashed lines in figure 5 reveal three darker areas that mark the limit of a P-rich zone that corresponds to some of the blobs visible in the POS, similar to the one pointed by the yellow arrow (Figs. 2, 5). These areas are highly enriched in P and delineate zones that extend beyond the POS. These darker areas are not discernable in the HAADF-STEM view, suggesting that they are of identical density to the surrounding less dark areas. We interpret the level of gray as a possible difference of crystal orientation within the OCL.

Co-bandings of sulfur and magnesium, as well as of S and P (or other elements assumed to reflect the presence of organic matter, such as N), have been documented in foraminifera (Paris et al., 2014b; Glock et al., 2019; van Dijk et al., 2019; Geerken et al., 2019; Lemelle et al., 2020). However, in detail, the relationships between the bands are variable. S-bands and P-bands tend to be sharper than Mg-bands in profiles across tests of the benthic foraminifera *Amphistegina lessonii* and *Ammonia tepida* (Geerken et al., 2019), while S-bands appear broader than Mg-bands in planktic foraminifera *Orbulina universa* (Paris et al., 2014a). In the last chamber of planktic foraminifera *Globorotalia menardii,* the S- and Mg-bands are very well correlated and similar in width, though S follows a pattern that is hybrid between P and Mg, with enrichments of all three elements in the POS (Lemelle et al. 2020). Here, S also displays a behavior that is hybrid between P and Mg distributions, with the same general organization. P and S follow a sharp band in the POS, while Mg is broader. Contrastingly, only P follows such a sharp pattern between the OOLs, while both Mg and S peaks tend to be more extended into the rest of the test. Here, ^{33}S enrichment is observed only in OCL$_{n-1}$, near the POS.

Finally, the coincidence between the different structures of the test and the composition is actually revealed through the superposition of TEM and NanoSIMS images. They reveal that the different OOL are associated to transition between chemical compositions more than they are associated to local maxima or minima. Overall, the comparison between the different results underline that NanoSIMS observations are more sensitive to chemical changes than by structures (as exemplified by OOLs or P/CaO maxima not associated with any change in density or diffraction in HAADF-STEM and bright-field TEM views, Fig. 6).

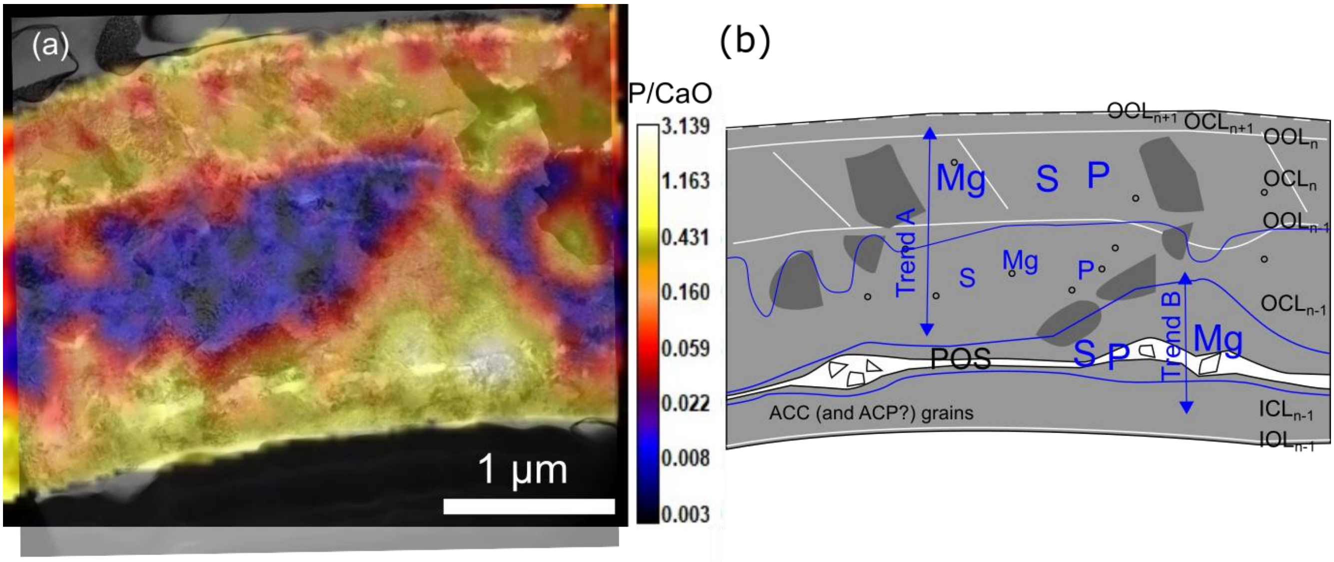

Figure 6. Superposition of the TEM view and the P/CaO map (a) and synthetic summary of the observations (b). In blue, information from the NanoSIMS analyses. The size of the letters reflect the relative abundance of the elements; trends A and B are from Fig. 4. White and gray reflect the TEM observations. The white lines are the POS associated with amorphous blobs as well as the OLs and the levels of gray from the CL, reflecting the change of orientation from one side and the other of OOL$_{n-1}$

3.3 P, Mg, S and Ca distribution in the cytoplasm

Cytoplasm remains attached to the test (see for instance Figs S4 and S5) display heterogeneities in the element distribution. More phosphorus and sulfur are observed in the organic matter located close to the test compared to the center of the cell. NanoSIMS images of the FIB lamella of the chamber (n-3) of the specimen F5(2)B and of the last chamber (n) of the specimen F2A (Fig. 7) reveal a notable degree of heterogeneity in the distribution of Ca, P, Mg and S in the cytoplasm. The cytoplasm contains areas that are strongly enriched in sulfur (^{33}S) (white arrows, Fig. 7d-e, 7j-i), which seems to correlate with relatively high sulfur (^{32}S) values in the final chamber (n) of the F2A specimen (Fig. 7k). Some large vesicles appear 'empty', because the original liquid inside the vesicles was emptied during the chemical fixation and the embedding in the epoxy resin and the process removes free ions. Some other large vesicles contain granular structures that are enriched in P, Ca and Mg (Fig. 7b,c,f green arrow) or in Ca and ^{33}S (Fig. 7i,j red arrow). Other smaller vesicle-like structures are rich in Mg, P and Ca (Fig. 7b, 7c and 7f, green arrow), or contain P, Ca, Mg and S (Fig. 7h,k,l, magenta arrows).

The CN, P and S maps enable us to trace a continuous layer, likely the inner organic layer (IOL), at the transition between the interior of the test and the endoplasm (the cytoplasm inside the cell) (Figs. 7a,b,e,g,h,k). Inside the cell, CN rich layers, possibly membranes, delineate the contour of vesicles-like structures. The inside of these vesicles can be grouped in three categories: seemingly "empty" (most likely because of the chemical fixation), enriched in P, Ca, Mg and moderately in S (green arrows in Fig. 7) or rich in Ca only (red arrow in Fig. 7).

Views of F5(2)B are focused on the wall between chambers 4 and 6 (or 7) and the cytoplasm inside chamber 3. The cytoplasm contains P, Mg and Ca-rich 2 µm grains (yellow arrow, Fig. 7b,c,e,f) and other smaller ones, ~ 0.5 µm (green arrows). They contain Ca, Mg, P, with moderate S-enrichment. Even though no strong S enrichment is seen in association with P, Ca and Mg, they are enriched in ^{33}S, showing that they contain seawater-sulfate, or seawater-sulfate derived sulfur. The maps of the final chamber of the F2A2 specimen reveal a more visible cytoplasmic area inside the test with large and small vesicle-like structures (Fig. 7g). The vesicles are generally poor in sulfur, while other areas of the cytoplasm and other unidentifiable organelles (structures), show pronounced ^{33}S enrichment (Fig. 7j). The 2-3 µm Ca-rich vesicle near the IOL of the last chamber of the FA2A specimen (Fig. 7g-k), though not enriched in sulfur (Fig. 7k), contains ^{33}S (Fig. 7j). Unlike the previously described structures, it does not contain phosphorus or Mg.

Free ions or free molecules have been removed during the fixation process, which suggests that the presence of calcium in association with phosphorus could be due to the presence of Ca-phosphate (Glock et al., 2025), while calcium alone could be Amorphous Calcium Carbonate. ACC is thought to occur in 5-µm vesicles *in Ammonia tepida* (de Nooijer et al., 2009) and *Amphistegina lessonii* (Dubicka et al., 2025), close to the size of the structure pointed by the red arrow (Fig. 7g-k). Interestingly, this structure seems to contain parts rich in Ca, close to the test, and parts rich in ^{33}S. The cytoplasm in the immediate vicinity of the vesicle is also richer in ^{33}S.

https://doi.org/10.5194/egusphere-2026-1505
Preprint. Discussion started: 26 March 2026

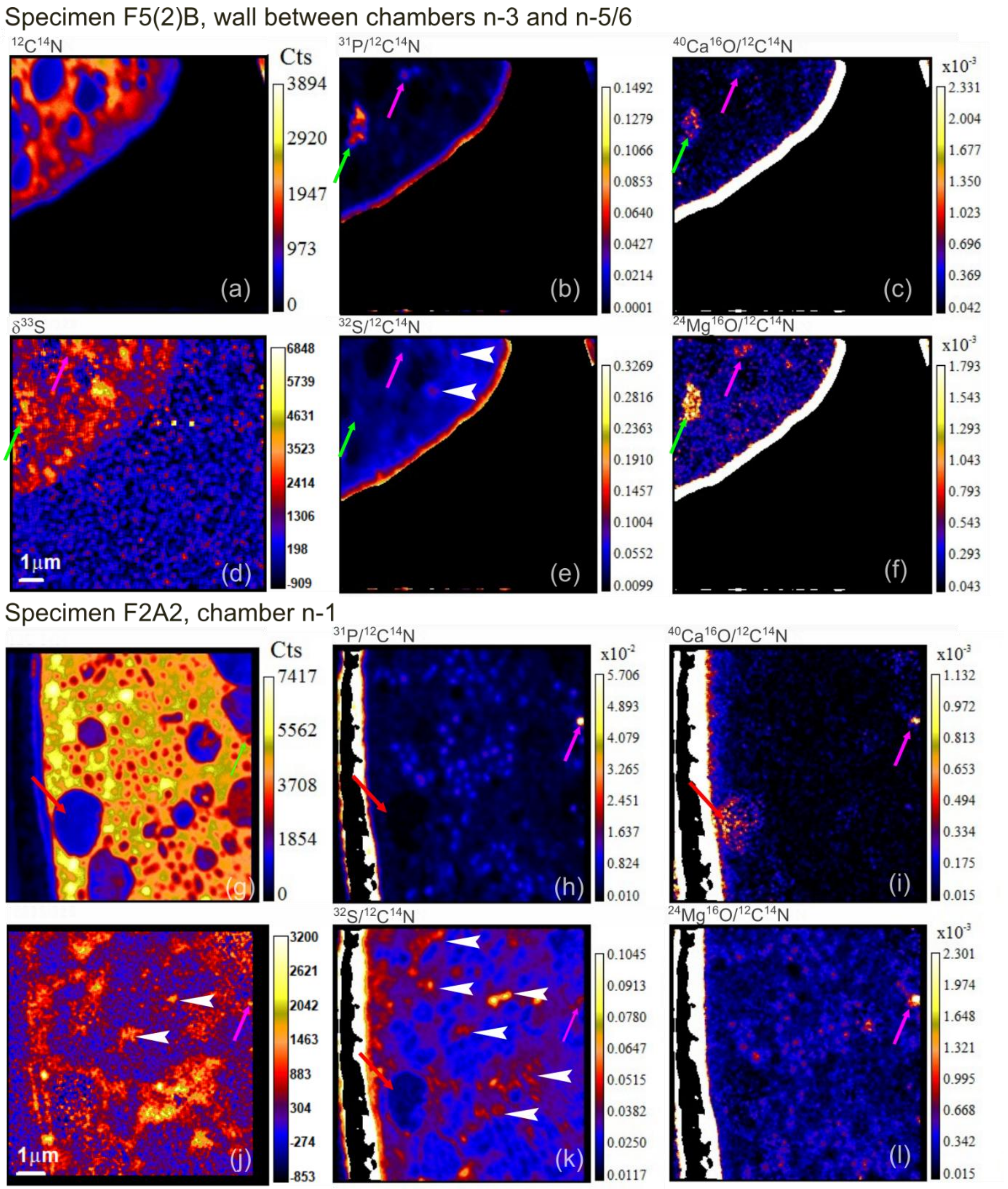

https://doi.org/10.5194/egusphere-2026-1505
Preprint. Discussion started: 26 March 2026

Figure 7. ^{14}C^{12}N, ^{31}P/^{14}C^{12}N, ^{40}Ca^{16}O/^{14}C^{12}N, δ^{33}S (‰), ^{32}S/^{14}C^{12}N and ^{24}Mg^{16}O/^{14}C^{12}N maps in the cytoplasm and test of chambers n-3 from foraminifera F5(2)B (a-f) and chamber n-1 from foraminifera F2A2 (g-l). A mask has been applied over the tests. The green arrow points to irregular P, Ca, Mg-rich 2 µm structures also enriched in ^{33}S, magenta arrows to ~0.5 µm grains rich in P, Mg, Ca and S, with ^{33}S enrichment. White arrowheads point to small (0.5-1µm) structures enriched in sulfur and ^{33}S and grey arrowheads follow a succession of Mg-rich grains. Inside the cell of F2A2, P-rich and S-poor grains can be observed, while S is enriched in between those grains. The red arrow points to a ~3-µm vesicle with Ca rich grains on the side close to test and ^{33}S rich on the other side. Position of the images with respect to the complete specimen are given in Fig. 1.

Images taken for specimen Fa5B reveal the path of sulfur from food through the trajectory of ^{33}S ingested with algae (reaching ratios of ~5%) along with unlabeled sulfur with natural δ^{33}S ratios within error (lower than ~100‰). The images reveal that in that case, labeled sulfur occurs as small grains within the cytoplasm, often enriched in Mg (grey arrowheads), but not systematically (blue arrowheads), not so much in Ca. This labeled sulfur is not found in the test, which did not grow during the culture experiment.

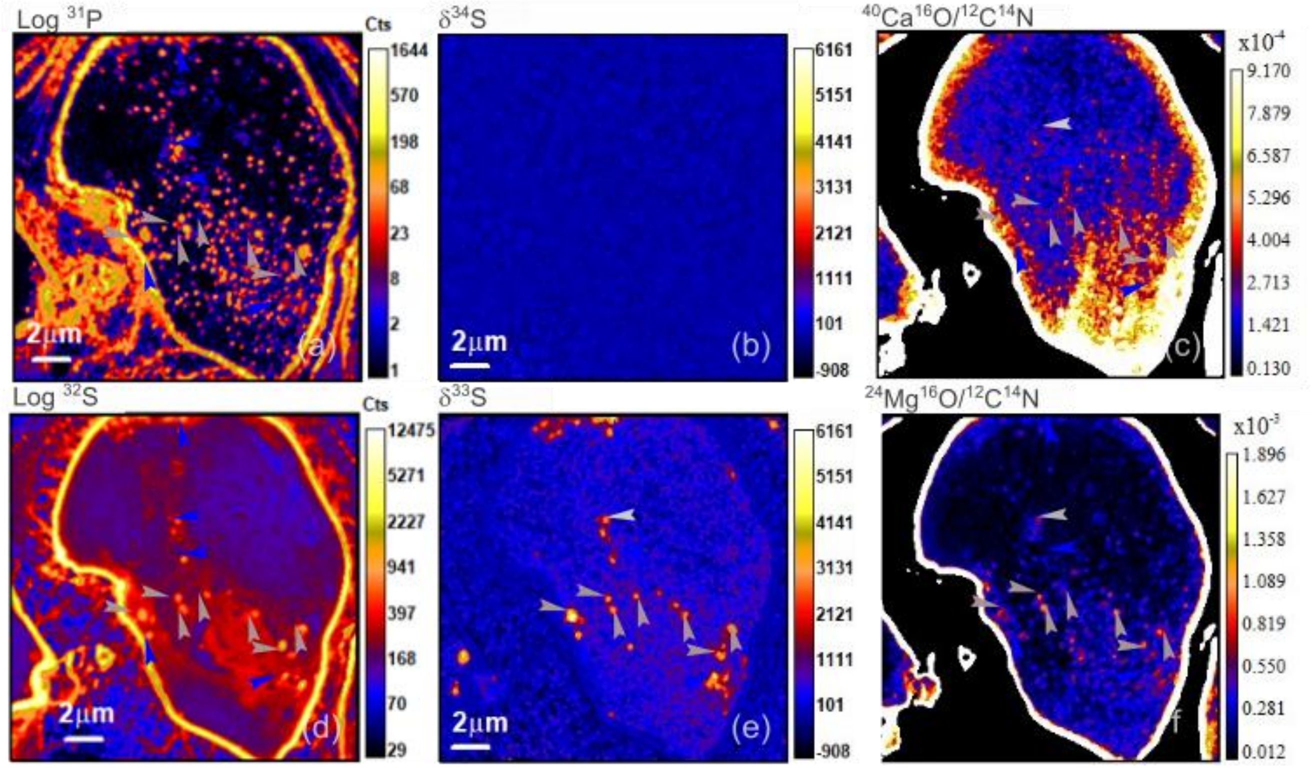

Figure 8. Log ^{31}P, δ^{34}S(‰) ^{40}Ca^{16}O/^{14}C^{12}N, Log^{32}S, δ^{33}S(‰) and ^{24}Mg^{16}O/^{14}C^{12}N maps in the cytoplasm and test of chamber n-1 from foraminifera Fa5B1 (a-f). A mask has been applied over the test in maps 8c and 8f. Grey arrowhead point to P, S, ^{33}S and Mg rich granules while blue arrowhead point to S and ^{33}S rich only granules

3.4 Sulfur isotope ratio values and incorporation of ^{33}S in the test

We produced maps of ^{32}S, ^{33}S and ^{34}S and analyzed isotope ratios (Fig. 10). Measured uncorrected δ^{34}S values range from to -13 ± 11 ‰ (1SD) to -1 ± 14 ‰ in calcite, while they range from -9 ± 8 ‰ to 13 ± 11 ‰ in organic matter, in the range of natural abundances. The δ^{34}S values we measured for sulfur present in the test are very close to that of the artificial seawater in which the foraminifera grew ($\delta^{34}S_{ASW}$ = 0.1 ‰, Thaler et al., 2023). Small differences may arise, but the analytical reproducibility (roughly ±8‰) and the absence of suitable reference materials do not allow us to investigate them. This confirms nonetheless that the instrumental mass fractionation (IMF) is likely small, within uncertainties; and that the corresponding correction can be neglected in the examination of $\delta^{33}S$ values that change widely because of the artificially increased amount of ^{33}S. The similar values between organic matter and calcite also indicates that matrix-related instrumental effects can be neglected in the following in regard to the observed variations and uncertainties. Clear variations of $\delta^{33}S$ values are observed, from 174 ± 28 to 5556 ± 68 ‰ in the test and from 1827 ± 44 to 3072 ± 36 ‰ in organic matter (Table 2). The values cannot be explained by a fractionation of such magnitude, which furthermore should have affected the $^{34}S/^{32}S$ ratios even more strongly. Whereas the values of $\delta^{34}S$ are similar in organic matter and calcite within errors, $\delta^{33}S$ values differ between these two components, with no systematic tendency. Instead, the observed values reflect a mixing between isotopically labeled (~7030 ‰) and non-labeled (~0 ‰) sulfur. We also note that the higher the $\delta^{33}S$ is in calcite, the higher it is also in organic matter.

Table 2. Summary of the average measured uncorrected $\delta^{34}S$ and $\delta^{33}S$ values of the test and organic matter (OM) of the samples analyzed only for the test.

FIB	image	$\delta^{34}S$ test	$\delta^{34}S$ OM	$\delta^{33}S$ test	$\delta^{33}S$ OM
A1(n-1)	20	-9 ± 6	-9 ± 6	5193 ± 70	2478 ± 23
A1(n)	21	-11 ± 11	-9 ± 8	5556 ± 68	3072 ± 36
F5(2)B1	23	-13 ± 12	13 ± 11	174 ± 28	1827 ± 44

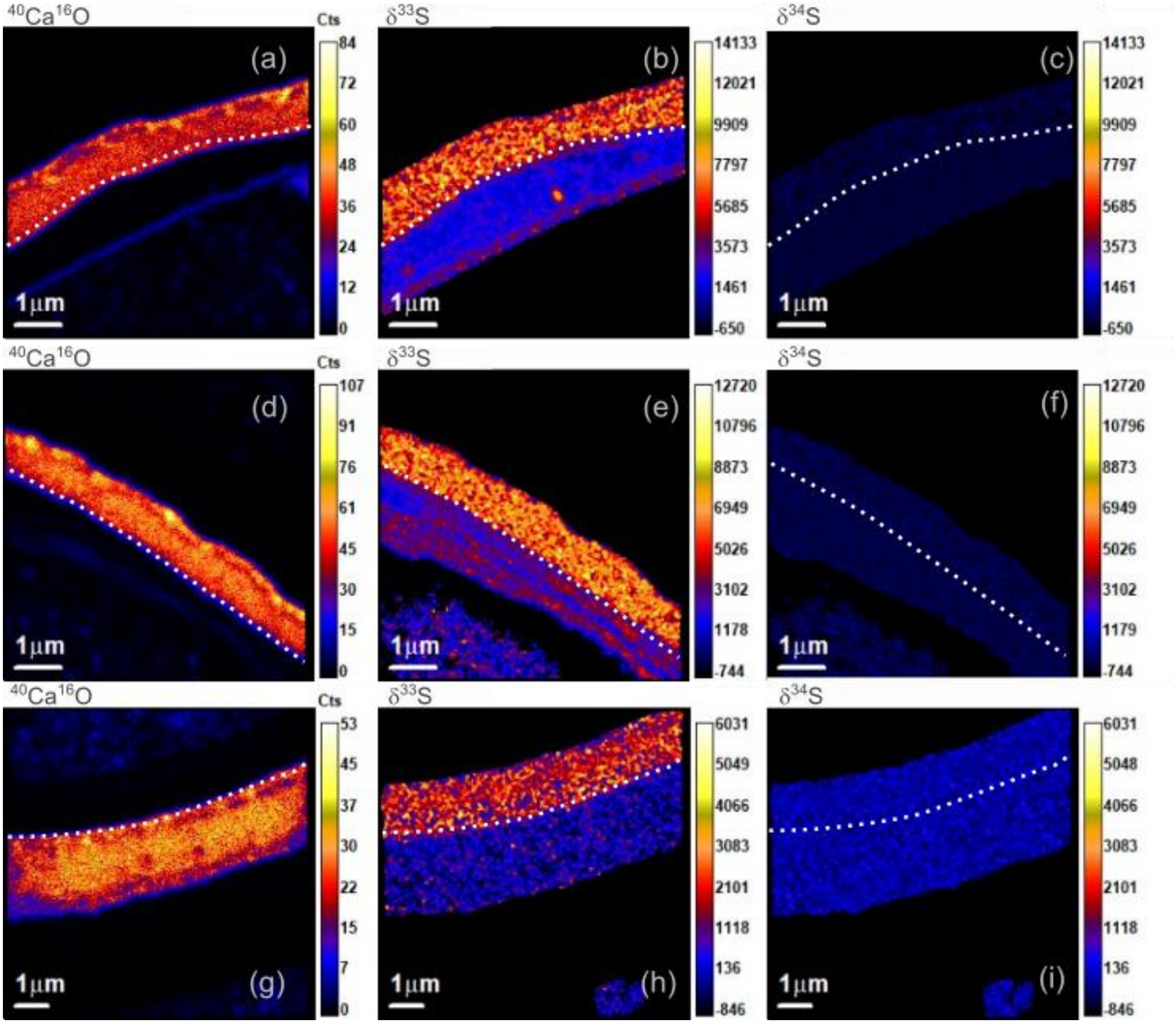

Figure 9. CaO, $\delta^{33}S$ and $\delta^{34}S$ maps across the walls of foraminifera A1 chamber n-1 (a,b,c) and n (d,e,f) and the wall of chamber n-1 of foraminifera F5(2)B (g,h,i). The dotted lines represent the limit between the test and the organic matter.

4. Discussion

4.1 Control of sulfate occurrence at the sites of biocalcification

Interpretation of $\delta^{33}S$ of the test depends first on the amount of calcite grown in labeled seawater. In most experiments, chambers formed before the foraminifera was transferred to the labeled seawater and the tests show little to virtually no ^{33}S enrichment (e.g., Fig 7h). Labeled sulfur can be found within the test, as well as within the organic matter of the last two chambers of specimen A1, which grew in labeled seawater (Fig. 7b, 7e, Table 2). The high values of $\delta^{33}S$ (~5300 ‰ in average) in both chambers suggests that ≈3/4 of the sulfur in the test comes from sulfate, which was taken up during the precipitation of the test from the calcification fluid derived from labeled ^{33}S seawater. Though some of the remaining sulfur is likely to be unlabeled organic sulfur, this number is a low estimate of the inorganic sulfate content of the test because chamber n-1 is slightly less enriched ($\delta^{33}S \approx 5190$ ‰) than the last chamber ($\delta^{33}S \approx 5560$‰). The difference between the two chambers could suggest that more labeled sulfate is incorporated in the last chamber, after the individual spent more time in labeled seawater. Thus, part of the incorporated sulfate could have been previously stored in the cell, and/or comes from the unlabeled food. However, the homogeneity of $\delta^{33}S$ values, that reveal no correlation with organic banding in the test, suggests that no significant amount of sulfur from food is present. The NanoSIMS image of the wall of the penultimate chamber of specimen F5(2)B (Fig. 5h) reveals that inside a chamber grown before being introduced to labeled seawater, the organic matter on the inner side of the test nevertheless contains ^{33}S, but that very little of this labeled sulfur is found in the test. New seawater sulfate is thus introduced in previously formed chambers, but no direct sulfate exchange occurs between previously formed calcite and seawater, at least on the outer edge of the test (Fig. 9).

Our observations shed new light on the tight control of sulfate in the cell. Rotaliid foraminifera are not only able to precipitate calcium carbonate but also to its composition and mineralogy. Three non-mutually exclusive processes have been described for charged ion transport to the site of biomineralization: seawater leak, transmembrane transport and seawater vacuolization (e.g. Erez, 2003; Bentov et al., 2009; Nehrke et al., 2013).

4.1.1 Seawater leak (SWL)

The biomineralization site is isolated from seawater through an extension of the pseudopodial network, part of the cytoskeleton, that extends out of the test of the foraminifera (Erez, 2003). This isolating layer has been suggested to be possibly open to external seawater at times, generating direct leaks to the site of biomineralization (Nehrke et al., 2013). As a result, seawater Ca, Mg and sulfate would make it directly to the sites of calcification. Such a leak could also explain the rapid incorporation of ^{33}S-labeled sulfate in the test. However, no labeled sulfur is found on the outside of previously formed test, which would suggest that this phenomenon does not occur any longer once the test is built, or that sulfate is somehow excluded from this leak. We see incorporation of seawater sulfate in walls from already built chambers during the experiment.

4.1.2 Trans-membrane transport (TMT).

A second model exists, based on the selective transport of Ca through the cell membranes, the TMT (trans-membrane transport). Coccolithophorids do not respond to calcein labeling, a molecule too big to go through membranes, which implies that calcite formation of coccolithophorids occurs entirely within intracytoplasmic compartments and requires TMT (Gussone et al., 2006; Langer et al., 2006, 2009; Nehrke et al., 2013). If TMT calcification occurs in foraminifera as well, the moderate but significant incorporation of sulfate inside the cytoplasm suggests that sulfate is actively pumped inside the cell. TMT could thus be coherent with the occurrence of ^{33}S in our observations. This suggests that, alongside vesicular transport, sulfate from seawater may enter the cell via transmembrane transport, possibly catalyzed by proteins of the sulfate permease (SulP) group. Though to our knowledge these proteins have not yet been identified in foraminifera, they belong to a large, ubiquitous family of proteins found in all kingdoms of life (Piłsyk and Paszewski, 2009). Many of these proteins function by SO_4^{2-}:H^+ symport, but SO_4^{2-}:HCO_3^-, or more generally, anion:anion antiport has been reported for several homologues (Piłsyk and Paszewski

2009). Such SulPs could enable the transport of sulfate across membranes, from the seawater to the cytosol, coherent with the global presence of ^{33}S in the cytoplasm and the organic matter (Fig. 9, 9).

4.1.3 Seawater vacuolization (SWV).

In this model, seawater is isolated in a portion of the membrane that detaches from the rest of the membrane and forms a vacuole full of seawater. The vacuole is transported all the way to the site of calcification as its pH and concentration in Ca, DIC and Mg are modified (Bentov et al., 2009; Bentov and Erez, 2006; Dellinger et al., 2018; Erez, 2003; Rollion-Bard and Erez, 2010; Weiner and Addadi, 2011). Vacuoles would also bring sulfate and magnesium, which would explain the rapid incorporation of ^{33}S-labeled sulfate into the test. In addition to transport as ions, Ca and DIC may be possibly transported as (high-Mg) amorphous calcium carbonate (Mg-ACC) granules (de Noojier et al., 2009; Dubicka et al. 2023, 2025). If the presence of SulP antiport were to be confirmed, export of sulfate from the vacuoles could contribute to the increase of pH and DIC as the seawater evolves, explaining the delivery of remaining sulfate to the test and the addition of sulfate to the cytoplasm. However, we cannot access the occurrence of ^{33}S or the elemental composition of the vesicles that would have contained seawater or modified seawater. They now may be part of the vesicles that appear "empty", because the liquid inside them would have been lost during the chemical fixation. The process indeed removes all free ions and small molecules from the cytosol or from within the vacuoles and organelles. We are thus unable to identify possible seawater vacuoles and provide further information on the SWV model.

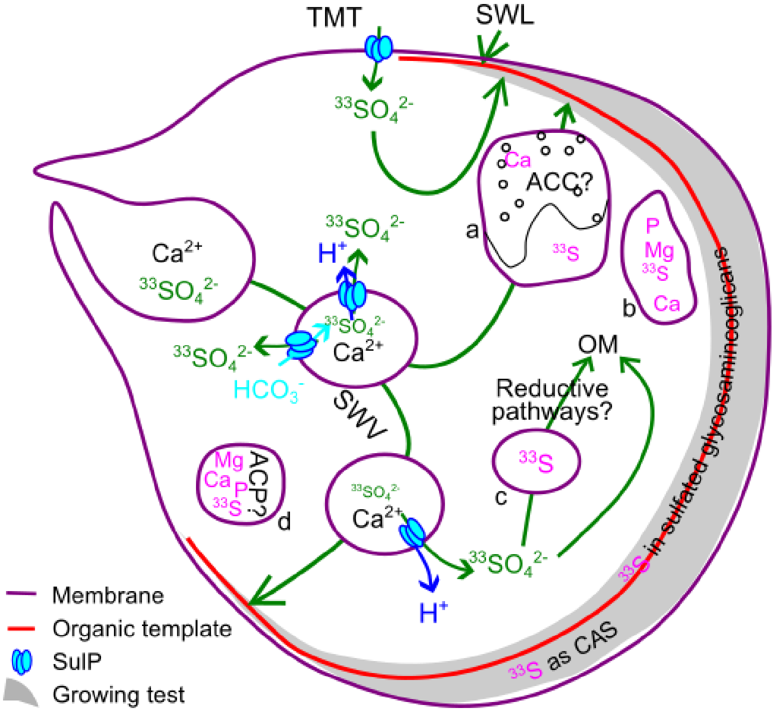

Figure 10. Schematic view of possible trajectories for labeled sulfur in the cell and co-occurrence with Mg, P and Ca. SulP = sulfate permease. SWL = seawater leak. TMT = trans-membrane transport. SWV=seawater vacuolization. ACC=Amorphous Calcium Carbonate. ACP=Amorphous Calcium Phosphate. a = vesicle containing Ca as ACC on one side and ^{33}S on the other. b=possible

autophagosome. c=electron opaque body or fibrillar vesicle. d=possible acidocalcisome. In green, possible pathways for labeled sulfate. In pink, observed location of elements by NanoSIMS. In dark and light blue, possible SulP paths for protons and HCO_3^-. Sulfate crosses membranes through SulP channels together with protons, contributing to increase the Ca/Mg and the CO_3/SO_4 ratios of the vesicles as the composition of the fluid increases. Some of these vesicles might be associated to ACC formation. In the cytoplasm, labeled sulfur may be stored as sulfate in fibrillar vesicles or electron opaque bodies, and possibly reduced and/or incorporated as sulfate in organic molecules such as sulfated glycosaminoglicans. In the mineral part of the test, labeled sulfur delivered to the site of biomineralization is included as Carbonate associated sulfate.

4.2 Sulfur and sulfate assimilation

From our experiments, we have the possibility to investigate the occurrence of fixed labeled sulfur in the cell (Fig. 7). The cytoplasm visible in the chemically fixed specimens, or the cellular material that remained attached to the test, is systematically enriched in ^{33}S. The $\delta^{33}S$ values imply a mixing of ~1/3 labeled and ~2/3 non-labeled sulfur (Table 2, Fig. 7). Higher labeled sulfur concentration occurs when the chamber effectively grew in the labeled artificial seawater. Organic matter close to the test displays average $\delta^{33}S$ values between 1800 and 3000 ‰ (Table 2), which indicate than ~1/4 of the sulfur comes from labeled sulfate and was thus taken from seawater during the duration of the experiment. For specimens F5(2)B3 and F2A2 (Fig. 7), for which the cell has been preserved and analyzed, we found average $\delta^{33}S$ values of 1932 ±36 (2σ) and 529 ±6 (2σ). This would correspond to ~25 % and ~7% of sulfur that originates from sulfate taken from seawater during the experiment. The higher incorporation of seawater sulfate here might reflect the fact that F5(2)B3 was cultivated at twice the sulfate concentration of F2A2 (Thaler et al., 2023).

In those experiments, the labeled sulfur is necessarily introduced in the cell as a free sulfate ion but the chemical fixation process applied to the cells removes small molecules and ions from the cell, such as ATP and free sulfate. Consequently, any remaining observable sulfur is thus either complexed or protein-bound. In consequence, our estimates of the relative proportion of seawater sulfate-sulfur in the cell could be underestimated. Regardless of this partial loss of information, labeled sulfate is present in the cytoplasm, where it is transported and incorporated in less than two to five days (the duration of culture in the labeled medium), despite the provision of unlabeled food. Such an addition of seawater sulfate is coherent with its important physiological roles. Sulfate is one of the most important anions in cells and plays a key role in maintaining ionic homeostasis and other vital functions, and therefore is considered as an essential macronutrient (Piłsyk and Paszewski, 2009).

When labeled sulfur comes from food, we only observe it in small grains within the cytoplasm, but we also observe a lot of sulfur enrichment that is not labeled (Fig. 8). The labeled sulfur is found in grains that are always rich in phosphate and often in Mg, but most P-rich grains are independent from sulfur.

In our experiment, there are thus at least two sources of sulfur: sulfate pumped from seawater and dietary sulfur. The combination of ^{33}S and ^{34}S data suggests that a significant proportion of the sulfur in the cytoplasm originates from food or previously stored seawater sulfate in pools, as it was suggested for inorganic carbon (ten Kuile and Erez, 1987; ter Kuile and Erez, 1988). These account for at most 75% of the sulfur present in the cytoplasm, even for foraminifera grown at higher sulfate concentrations (i.e., $[SO_4^{2-}]$ = 56.36 mmol L^{-1} for F5(2)B). Combined observations in foraminifera F5(2)B and Fa5B indicate that sulfur in the cytoplasm comes from dietary sulfur from or sulfate pools stored in the cell before the labeled growth, or a combination of both. Our observation cannot confirm the occurrence of sulfate assimilatory reduction within the cell and because either seawater sulfate or food could have been ingested before the labeling experiments, some uncertainty remains in our interpretations.

Regardless, the presence of labeled sulfur in the cell is coherent with the fact that physiological activity of foraminifera, at least some benthic species, requires sulfate (Jauffrais et al., 2019; LeKieffre et al., 2022; Thaler et al., 2023) and within the cytoplasm of the cell, we observe ^{33}S-rich granular-like structures (white arrows Fig. 7). Sulfur enrichments in the kleptoplastic benthic foraminifera *Nonionellina labradorica,* as well as in *Bulimina marginata*, *Cassidulina laevigata*, *Haynesina germanica*, *Ammonia* sp. and *Elphidium williamsoni* have also been proposed to occur in fibrillar vesicles or electron-opaque bodies that also contain N (both smaller than 0.5 µm) or unidentified structures that are 2-5 µm big (LeKieffre et al., 2022). Here, the grains are smaller than 0.5 µm and could correspond to these fibrillar vesicles or electron opaque bodies previously described (Fig. 10). However, we cannot discriminate between reduced and oxidized sulfur and thus use our data to support the occurrence of sulfate assimilation observed in different species of foraminifera (Jauffrais et al., 2019; LeKieffre et al., 2022; Nomaki et al., 2016).

4.3 Ultrastructure of the test and distribution of Mg, S and P: organic or inorganic banding?

In detail, two trends can be found in the correlations between those elements within the tests (Fig. 4) with S, P and Mg all varying simultaneously. Trend A is found across OCL_n and OCL_{n-1}, is not impacted by the presence of the OOL (see figures 3 and 7) and most likely corresponds to the Mg-banding that has been thoroughly investigated over the years (e.g., Eggins et al., 2004; Kunioka et al., 2006; Spero et al., 2015b; Fehrenbacher et al., 2017). Mg is inorganically present in foraminiferal calcite (Branson et al., 2013), which is expected due to its incorporation as an impurity in inorganic calcite, affecting calcite solubility and stability (Alkhatib et al., 2022; Mavromatis et al., 2013; Mucci, 1987; Saulnier et al., 2012). Occurrence of sulfate as an inorganic ion is expected as well, because sulfate is also incorporated in inorganically precipitated calcite (Barkan et al., 2020; Busenberg and Plummer, 1985; Fernández-Díaz et al., 2010; Goetschl et al., 2019; Kitano et al., 1975; Kontrec et al., 2004). The observed Mg-S covariation could be due to changes in precipitation rates, as higher rates translate into higher Mg- and SO_4-incorporation into the mineral lattice (Alkhatib et al., 2022; Barkan et al., 2020; Busenberg and Plummer, 1985; Mavromatis et al., 2013), though incorporation of sulfate reduces the possibility to incorporate magnesium (Goetschl et al., 2019). In this pattern, P variations could also be inorganically driven, as phosphate also is included in calcite as an impurity (House and Donaldson, 1986; Plant and House, 2002; Ren et al., 2021). Though phosphorus is traditionally interpreted as reflecting the occurrence of organic matter, trend A is thus likely mostly inorganically driven regarding that the last outer calcitic layer, delimited by the OOL_n and OOL_{n-1}, is more P-enriched than the OOL themselves.

On the other hand, trend B represents P, Mg and S enrichments across the POS and possibly extends into the OCL. It could be explained by the presence of organic matter that contains S, Mg and P. Sulfur is known to be present in sulfated glycosaminoglycans present in the POS (Angell, 1967; Bé et al., 1979; Dauphin et al., 2008; Hemleben et al., 1986; Spero, 1998; Weiner and Erez, 1984) and enrichment of Mg (and Na) in the POS of *O. universa* has been interpreted as a contribution of organically carried Mg (Branson et al., 2016), supporting earlier interpretation of an association of Mg to organic matter (Erez, 2003; Kunioka et al., 2006). In this case, trend B could be due to the co-occurrence of S, Mg and P in organic matter, though this hypothesis is not supported by the distribution of P, S and Mg enrichments into the test way past the POS or independently from the OOLs. Indeed, the P, S and Mg enrichment is wider than the white lines observed in the TEM view. This observation is consistent with previous investigations (e.g. Branson et al., 2016; Lemelle et al., 2020), though here we suggest that organic matter might not be the common carrier. Indeed, the bright-field TEM views overall reveal amorphous/organic linings as thin white lines, the HAADF imaging reveals them as equally sharp less dense areas. Contrastingly, NanoSIMS maps follow a coherent but broader pattern that is not explainable by the difference of resolution between the methods (Fig. 6). Phosphorus, S and Mg defines clearly broader areas that the white lines and the areas that are the most enriched in P, S and Mg appear centered on non-crystalline blobs within the POS (Fig. 2, 5, 6).

Within the outer calcitic layers (Fig. 5, 6), locally dark local (less crystalline or with a different orientation) are associated with a transition from high to low P, Mg and S levels. In between those areas are P, Mg and S-rich zones associated with brighter zones, which seem to extend into the calcitic layer. However, HAADF-STEM observations reveal no detectable change in density, and thus probably not a change in OM content. Instead, they are more consistent with changes in crystallinity and/or crystal orientation and amount of impurity in calcite rather than a phase change. Altogether these observations lead to questioning the generally assumed correlation between organic matter and phosphorus distribution in foraminiferal tests. Instead, P, S and Mg all likely reflect a combination of processes that could be related to the amorphous biomineralization pathway. Furthermore, the use of composition maps without fine observations of test ultrastructure may lead to misinterpretation of P and S bandings as organic linings. This conclusion however may not apply to the IOL that does appear to be the richest parts of the cell in both S and P (Fig. 8), though this is hard to properly constrain due to the obvious change in matrix from cytoplasm to test.

Overall, our observations could support that organic sulfur in the IOL or the test is not sourced from food. The lack of ^{33}S-poor banding in the test of chambers that grew in labeled seawater also supports that dietary sulfur does not play an important role in test building (Fig. 9). In figure 8, the chamber grew before foraminifer has been fed with labeled algae, which could explain the lack of labeled sulfur in the test. Contrastingly, the moderate, yet unambiguous presence of labeled sulfur in a test not grown in labeled seawater (Fig. 4, 5) suggests that some seawater-sulfur, unlike dietary sulfur, is incorporated in previously built chambers.

4.4 Implication for biocalcification processes: Amorphous calcium carbonate (and phosphate) pathway(s)?

Non-crystalline structures within the POS or the grains of the OCL could be grains of Amorphous Calcium Carbonate (ACC). ACC is a family of disordered phases more or less hydrated (Cartwright et al., 2012), likely to occur as a transitory precursor phase in many calcifying organisms, including foraminifera (Addadi et al., 2003; Arns et al., 2022; Bentov et al., 2010; De Yoreo et al., 2015; Dubicka et al., 2023; Gilbert et al., 2022; Jørgensen et al., 1985; Lemelle et al., 2020; de Nooijer et al., 2014; Weiner et al., 2003). Vaterite has also been suggested as a precursor to foraminiferal calcite (Jacob et al., 2017). The nanogranular structures (Fig. 2) we observe in the OCLs could also be ACC nanograins within the OCL are consistent with previous work that reveals the occurrence or ACC or nanocrystals through the test (Arns et al., 2022).

Instead of the presence of organic matter, the co-distribution of S, Mg and P (trend B) could reflect their combination in controlling ACC formation, stability and/or ACC-calcite transition. The co-occurrence of ACC and phosphate could also be partly explained by the role of polyphosphate molecules, notably phospho-amino acids, that play a role in the induction of ACC formation in organisms such as crayfish (Bentov et al., 2010; Weiner et al., 2003). Phosphate could also occur as inorganic phosphate ions that can also promote the crystallization of calcite from ACC because they prevent vaterite formation (Zou et al., 2021). Calcium-phosphate grains could also be hypothesized to occur in the test, as a way to store phosphate away from the growing calcite. Similarly, though Mg is likely to reduce the ability to form ACC at seawater Mg/Ca ratios (Evans et al., 2019), it increases the stability of ACC (Dubicka et al., 2023, 2025; Evans et al., 2020) and favors the formation of calcite over vaterite (Rodriguez-Blanco et al., 2012). Finally, sulfate as well plays many roles in controlling ACC or $CaCO_3$ minerals that precipitate, whether calcite, and aragonite but also vaterite (Bots et al., 2012; Fernández-Díaz et al., 2010).

We thus hypothesize here that phosphate, Mg and SO_4^{2-} all contribute to ACC formation and/or stabilization, just like they do in calcite and aragonite precipitation. We also assume that they are all easily incorporated in ACC. For instance, Mg is incorporated in ACC twice as much as in calcite (Evans et al., 2020; Raz et al., 2000). The incorporation of sulfate in ACC formation is not documented yet, but the similarity of patterns with Mg and P could be due to the need to control them in the precipitation fluid and in the growing calcium carbonate. This could also explain why P, S, Mg as well as other elements are distributed more broadly than the POS, if the stabilization of calcite implies progressive removal of the ionic impurities. Furthermore, the nanogranular structure we observe in the OCLs (Fig. 2) could possibly be interpreted as the occurrence of small ACC grains in the test, because such small grains can be observed within the OLs (Fig. 2e) and extend into the OCLs. Alternatively, they could be interpreted as fluid inclusions within the test because the transition from ACC to calcite that will likely occur with a dehydration and decrease of volume (Bots et al., 2012; Cartwright et al., 2012).

In the cytoplasm, the presence of ACC could explain the Ca-rich vesicle observed in specimen F2A2 (Fig 7i), as ACC is known to occur in 5-µm vesicles in *A. tepida* (de Nooijer et al., 2009;) and *A. lessonii*, where have been suggested to be directly incorporated in the growing test Dubicka et al., 2023, 2025. The possible grain of ACC (red arrow Fig. 7, Fig. 10), similar in size as observations from de Nooijer et al. (2009) or Dubicka et al. (2023, 2025), appears associated with S removal, as indicated by the separation between Ca and ^{33}S. In this scenario, the intervention of SulP proteins could remove sulfate and add carbonate or remove sulfate and protons. It is also noteworthy that Ca is often associated to P enrichment in the cytoplasm. P-rich structures have been observed in *Ammonia veneta* and *Bolivina spissa* (Glock et al., 2025). In *B. spissa,* they were interpreted as granules of Ca polyphosphates. In *A. veneta*, P was found to accumulate in vesicles 0.5–2.0 µm in diameter, not unlike the size of what can be observed in the cell of F5(2)B3 (Fig. 7 a-f) or F2A2 (Fig. 7 g-l). Structures of similar size have been described and interpreted as either acidocalcisomes or autophagosomes (Glock et al., 2025; Goodenough et al., 2019). Autophagosomes accumulate Ca-polyphosphates and are described as irregular in shape (Docampo and Moreno, 2011; Glock et al., 2025). They could correspond to the less regular structures observed in F5(2)B3 (green arrow). Acidocalcisomes are membrane-enclosed organelles, close to 0.5 µm in size, that accumulate granular phosphate and inorganic polyphosphate, as well as calcium as ACP (Amorphous Calcium Phosphate) or magnesium and metals. They contribute to Ca storage and homeostasis as well as to intracellular pH and osmotic regulation (Docampo et al., 2005; Docampo and Moreno, 2011; Goodenough et al., 2019). The smaller vesicle in F2A2 (magenta arrow) could thus be an acidocalcisome. In all cases, these organelles are likely to contain ACP (Fig. 10).

The regulation and transport of Ca in the cell possibly take different forms, including ACC and ACP. Phosphate could thus be active in biomineralization processes of rotaliid foraminifera and play active roles as an inorganic ion, not only as a part of organic matter or ATP. ACP indeed has been demonstrated to play an important role in urchin spicule or coccolith calcite precipitation (Kahil et al., 2021). Taken together, our observations could also support the occurring of ACP in the test in combination to ACC as another contributor to trend B and the P-enrichments observed in non-crystalline grains. It also suggests a different role of ACC and ACP in the cytoplasm (storage, transport) than in the test (active part of the biomineralization process).

4.5 Implications for CAS as a proxy

Most (if not all) of the sulfate in the test comes ultimately from seawater, as supported by the ^{33}S labeling experience, whether through SWV, SWL or TMTs. Such a result, associated with small fractionation during carbonate precipitation (Barkan et al., 2020) contributes to explain why foraminifera appear as robust recorder of seawater δ^{34}S values (Burdett et al., 1989; Paris et al., 2014a; Rennie et al., 2018; Thaler et al., 2023). However, though the S/Ca ratio in foraminifera has been suggested to reflect seawater carbonate ion concentration (Boyle et al., 2002; van Dijk et al., 2017, 2019b), it is probably not linked to a direct precipitation from seawater itself, but instead might result from a complex mechanism, involving Ca-, Mg-, CO_3^{2-} and SO_4^{2-} control. In the absence of further constraints, and assuming that SulP are present in the cell, we could speculate that pH and Dissolved Inorganic Carbon regulation necessary to calcite formation involves SO_4^{2-}:H^+ symport or SO_4^{2-}:HCO_3^-antiport SulP proteins that could alter the SO_4/CO_3 content of the precipitating material to the initial seawater, as well as the Mg/Ca ratio, more or less depending on the initial seawater pH. Furthermore, the POS in tests that grew in labeled seawater does not appear to correspond to lower ^{33}S values, which suggests that the sulfate in the POS would also come from seawater, and not from the food. Thus, organically bound sulfate that occurs in the POS may also bear the δ^{34}S value of seawater, unless a fractionation is shown to occur as sulfate is incorporated into sulfated glycosaminoglycans. As a result, the sulfur isotope signature of CAS may be unaffected by the integration of the organic matter from the test itself. It could, however, be modified by the integration of OM from the cytoplasm, which contains reduced sulfur with a distinct isotopic signature (Thaler et al., 2023). Indeed, most (dissimilatory) sulfate reducing processes tend to generate lower isotopic ^{34}S/^{32}S ratios in the reduced product, which would imply that sulfur in organic matter has a lower δ^{34}S value than the initial sulfate available (e.g., Habicht et al., 2002; Farquhar et al., 2003; Crowe et al., 2014; Gomes and Hurtgen, 2015; Sim et al., 2023). As a result, removal of organic matter included within the test may be of lesser importance for the interpretation of δ^{34}S values than the removal of the cytoplasm.

5. Conclusion

Cells were cultured in ^{33}S-labeled seawater to document the origin of sulfur in the calcitic test and the cytoplasm of the rotaliid benthic foraminifera. Chambers that grew in ^{33}S-labeled seawater revealed that at least 1/3 of the sulfate incorporated is directly taken from seawater. Thanks to a fixation process that gives access to both the test and the cytoplasm, we revealed that ^{33}S-labeled seawater is also found within the cytoplasm and document the distribution of Ca, S, Mg and P. In addition, a combination of TEM bright-field, HAADF-STEM imaging and NanoSIMS analysis highlights the general co-occurrence of Mg, S and P according to the ultrastructure of the test chambers. These elements appear to be concentrated in two areas, primarily near the primary organic sheet (POS) and within the last-deposited outer calcitic layer. Non-crystalline grains can be found in the parts of the POS that are richest in P, Mg and S, and within the organic calcitic layers and could contain ACC and ACP. ^{33}S-labeled sulfur is present in a test that grew up in seawater, indicating direct incorporation of seawater sulfate with calcium and carbonate ions, independently of the structure of the organic layers. Finally, µm-scale grains can be found in the cytoplasm. A Ca-rich grain, approximately 3 µm big, can be interpreted as ACC-containing vesicle, while smaller grains (less than 1 µm) Ca, Mg and P rich and can be interpreted as autophagosomes or acidocalcisome that contain calcium phosphate, possibly amorphous.

Sulfate incorporation and its occurrence at the sites of mineralization are thus most likely closely controlled by the cell. Such control might occur through the use of Ca^{2+} or alkalinity pumps, that would decrease the relative abundance of sulfate compared to Ca^{2+} or CO_3^{2-} but could also involve active proteins, likely of the Sulfate permease family. Regulation of sulfate is necessary for foraminifera, possibly due to the assimilation of sulfate and to the control of the biomineral phase that precipitates. Indeed, sulfate also plays a role in precursor precipitation and stabilization. Together with magnesium and phosphate, sulfate play many roles in controlling ACC or the polymorphs of $CaCO_3$ that precipitate, whether calcite, and aragonite and even vaterite. SulfP proteins could thus be involved in the evolution of seawater/biomineralizing fluid composition in vacuoles or at the sites of precipitation, to control the presence of sulfate in the POS, and the amount of sulfate in interaction with ACC or calcite. Though we cannot confirm the occurrence of an assimilatory pathway for sulfur in foraminifera we investigated, the clear presence of sulfur from seawater in the cell demonstrates that sulfate is involved in many aspects of foraminifera biological activity, in close association with Ca-transportation, Mg and P distribution, and likely with ACC, as well as possibly ACP, formation and evolution.

Author contributions

AC, GP and CT designed the experiments and observations. Growth experiments were led by CT and MD. NanoSIMS analyses and data processing were performed by CT, AC, JA, and SM. FIB sections were extracted by DT. TEM observations were performed by GYW and AC. GP interpreted the data and wrote the paper with AC and contributions from all co-authors.

Competing interests

The authors declare that they have no competing interests

Acknowledgements

This research was funded by the LabEx BCDiv project “SULFOR, Impact of SO_2 on ocean acidification and foraminiferal biocalcification” (PI Annachiara Bartolini), CNRS INSU INTERRVIE project “Impact of sulfate variations on the biocalcification of foraminifera” (PI Annachiara Bartolini); Paris Ile-de-France Region – DIM “Patrimoines matériels – innovation, expérimentation et resilience” through the project POLIMO “Projet d’Observation aux Limites des Interactions Minéral / Organique à l’échelle cellulaire” (PI Claire Rollion-Bard and Annachiara Bartolini). The National NanoSIMS facility at the Muséum National d'Histoire Naturelle is funded by CNRS, Région Île de France, Ministère délégué à l'Enseignement supérieur et à la Recherche, and the Muséum National d'Histoire Naturelle and is part of the RéGEF network. FIB experiments were supported by the French RENATECH network, the CPER Hauts de France project IMITECH and the Métropole Européenne de Lille.

Financial support

Support funds and grant agreement numbers are listed as specified upon manuscript registration and reported to FundRef upon publication.

Data availability

All TEM/STEM original files are available online: https://doi.org/10.24396/ORDAR-230. Other data are provided in the supplementary material.

References

Addadi, L., Moradian, J., Shay, E., Maroudas, N. G., and Weiner, S.: A chemical model for the cooperation of sulfates and carboxylates in calcite crystal nucleation: Relevance to biomineralization, Proceedings of the National Academy of Sciences, 84, 2732–2736, 1987.

Addadi, L., Raz, S., and Weiner, S.: Taking Advantage of Disorder: Amorphous Calcium Carbonate and Its Roles in Biomineralization, Advanced Materials, 15, 959–970, https://doi.org/10.1002/adma.200300381, 2003.

Aléon-Toppani, A., Brunetto, R., Aléon, J., Dionnet, Z., Rubino, S., Levy, D., Troadec, D., Brisset, F., Borondics, F., and King, A.: A preparation sequence for multi-analysis of µm-sized extraterrestrial and geological samples, Meteoritics & Planetary Science, 56, 1151–1172, https://doi.org/10.1111/maps.13696, 2021.

Alkhatib, M., Qutob, M., Alkhatib, S., and Eisenhauer, A.: Influence of precipitation rate and temperature on the partitioning of magnesium and strontium in calcite overgrowths, Chemical Geology, 599, 120841, https://doi.org/10.1016/j.chemgeo.2022.120841, 2022.

Angell, R. W.: The Test Structure and Composition of the Foraminifer Rosalina floridana*, The Journal of Protozoology, 14, 299–307, https://doi.org/10.1111/j.1550-7408.1967.tb02001.x, 1967.

Arns, A. I., Evans, D., Schiebel, R., Fink, L., Mezger, M., Alig, E., Linckens, J., Jochum, K. P., Schmidt, M. U., Jantschke, A., and Haug, G. H.: Mesocrystalline Architecture in Hyaline Foraminifer Shells Indicates a Non-Classical Crystallisation Pathway, Geochemistry, Geophysics, Geosystems, 23, e2022GC010445, https://doi.org/10.1029/2022GC010445, 2022.

Barkan, Y., Paris, G., Webb, S. M., Adkins, J. F., and Halevy, I.: Sulfur isotope fractionation between aqueous and carbonate-associated sulfate in abiotic calcite and aragonite, Geochimica et Cosmochimica Acta, 280, 317–339, https://doi.org/10.1016/j.gca.2020.03.022, 2020.

Bé, A. W. H., Hemleben, C., Anderson, O. R., and Spindler, M.: Chamber Formation in Planktonic Foraminifera, Micropaleontology, 25, 294–307, https://doi.org/10.2307/1485304, 1979.

Bentov, S. and Erez, J.: Impact of biomineralization processes on the Mg content of foraminiferal shells: A biological perspective, Geochemistry, Geophysics, Geosystems, 7, Q01P08, https://doi.org/10.1029/2005gc001015, 2006.

Bentov, S., Brownlee, C., and Erez, J.: The role of seawater endocytosis in the biomineralization process in calcareous foraminifera, Proceedings of the National Academy of Sciences, 106, 21500–21504, https://doi.org/10.1073/pnas.0906636106, 2009.

Bentov, S., Weil, S., Glazer, L., Sagi, A., and Berman, A.: Stabilization of amorphous calcium carbonate by phosphate rich organic matrix proteins and by single phosphoamino acids, Journal of Structural Biology, 171, 207–215, https://doi.org/10.1016/j.jsb.2010.04.007, 2010.

Berner, R. A. and Canfield, D. E.: A new model for atmospheric oxygen over Phanerozoic time, American Journal of Science, 289, 333, 1989.

Bots, P., Benning, L. G., Rickaby, R. E. M., and Shaw, S.: The role of SO4 in the switch from calcite to aragonite seas, Geology, 39, 331–334, https://doi.org/10.1130/G31619.1, 2011.

Bots, P., Benning, L. G., Rodriguez-Blanco, J.-D., Roncal-Herrero, T., and Shaw, S.: Mechanistic Insights into the Crystallization of Amorphous Calcium Carbonate (ACC), Crystal Growth & Design, 12, 3806–3814, https://doi.org/10.1021/cg300676b, 2012.

Boyle, E., Berry, J., Erez, J., and Tishler, C.: Sulfur in foraminifera shells, a new paleoceanographic proxy for carbonate ion in seawater, AGU Fall Meeting Abstracts, PP52B-13, 2002.

Branson, O., Redfern, S. A. T., Tyliszczak, T., Sadekov, A., Langer, G., Kimoto, K., and Elderfield, H.: The coordination of Mg in foraminiferal calcite, Earth and Planetary Science Letters, 383, 134–141, https://doi.org/10.1016/j.epsl.2013.09.037, 2013.

Branson, O., Bonnin, E. A., Perea, D. E., Spero, H. J., Zhu, Z., Winters, M., Hönisch, B., Russell, A. D., Fehrenbacher, J. S., and Gagnon, A. C.: Nanometer-Scale Chemistry of a Calcite Biomineralization Template: Implications for Skeletal Composition and Nucleation, Proceedings of the National Academy of Sciences, 113, 12934–12939, https://doi.org/10.1073/pnas.1522864113, 2016.

Bryant, R. N., Richardson, J. A., Kalia, T. C., Gros, O., Lopez-Garriga, J., and Blättler, C. L.: Inorganic sulfate–based signatures of chemosymbiosis in modern infaunal lucinids, Geology, 2023.

Burdett, J. W., Arthur, M. A., and Richardson, M.: A Neogene seawater sulfur isotope age curve from calcareous pelagic microfossils, Earth and Planetary Science Letters, 94, 189–198, https://doi.org/10.1016/0012-821X(89)90138-6, 1989.

Burton, E. A. and Walter, L. M.: The role of pH in phosphate inhibition of calcite and aragonite precipitation rates in seawater, Geochimica et Cosmochimica Acta, 54, 797–808, https://doi.org/10.1016/0016-7037(90)90374-T, 1990.

Busenberg, E. and Plummer, L. N.: Kinetic and thermodynamic factors controlling the distribution of SO32− and Na+ in calcites and selected aragonites, Geochimica et Cosmochimica Acta, 49, 713–725, https://doi.org/10.1016/0016-7037(85)90166-8, 1985.

Canfield, D. E. and Raiswell, R.: The evolution of the sulfur cycle, American Journal of Science, 299, 697–723, https://doi.org/10.2475/ajs.299.7-9.697, 1999.

Cartwright, J. H. E., Checa, A. G., Gale, J. D., Gebauer, D., and Sainz-Díaz, C. I.: Calcium Carbonate Polyamorphism and Its Role in Biomineralization: How Many Amorphous Calcium Carbonates Are There?, Angewandte Chemie International Edition, 51, 11960–11970, https://doi.org/10.1002/anie.201203125, 2012.

Claypool, G. E., Holser, W. T., Kaplan, I. R., Sakai, H., and Zak, I.: The age curves of sulfur and oxygen isotopes in marine sulfate and their mutual interpretation, Chemical Geology, 28, 199–260, https://doi.org/10.1016/0009-2541(80)90047-9, 1980.

Coplen, T. B. and Krouse, H. R.: Sulphur isotope data consistency improved, Nature, 392, 32–32, https://doi.org/10.1038/32080, 1998.

Craddock, P. R., Rouxel, O. J., Ball, L. A., and Bach, W.: Sulfur isotope measurement of sulfate and sulfide by high-resolution MC-ICP-MS, Chemical Geology, 253, 102–113, https://doi.org/10.1016/j.chemgeo.2008.04.017, 2008.

Crowe, S. A., Paris, G., Katsev, S., Jones, C., Kim, S.-T., Zerkle, A. L., Nomosatryo, S., Fowle, D. A., Adkins, J. F., Sessions, A. L., Farquhar, J., and Canfield, D. E.: Sulfate was a trace constituent of Archean seawater, Science, 346, 735–739, https://doi.org/10.1126/science.1258966, 2014.

Cuif, J.-P., Dauphin, Y., Doucet, J., Salome, M., and Susini, J.: XANES mapping of organic sulfate in three scleractinian coral skeletons, Geochimica et Cosmochimica Acta, 67, 75–83, https://doi.org/10.1016/S0016-7037(02)01041-4, 2003.

Cusack, M., Dauphin, Y., Cuif, J.-P., Salomé, M., Freer, A., and Yin, H.: Micro-XANES mapping of sulphur and its association with magnesium and phosphorus in the shell of the brachiopod, Terebratulina retusa, Chemical Geology, 253, 172–179, https://doi.org/10.1016/j.chemgeo.2008.05.007, 2008.

Dauphin, Y., Cuif, J.-P., Doucet, J., Salomé, M., Susini, J., and Terry Willams, C.: In situ chemical speciation of sulfur in calcitic biominerals and the simple prism concept, Journal of Structural Biology, 142, 272–280, https://doi.org/10.1016/S1047-8477(03)00054-6, 2003.

Dauphin, Y., Cuif, J.-P., Salomé, M., and Susini, J.: Speciation and distribution of sulfur in a mollusk shell as revealed by in situ maps using X-ray absorption near-edge structure (XANES) spectroscopy at the S K-edge, American Mineralogist, 90, 1748–1758, https://doi.org/10.2138/am.2005.1640, 2005.

Dauphin, Y., Cuif, J.-P., and Williams, C. T.: Soluble organic matrices of aragonitic skeletons of Merulinidae (Cnidaria, Anthozoa), Comparative Biochemistry and Physiology Part B: Biochemistry and Molecular Biology, 150, 10–22, https://doi.org/10.1016/j.cbpb.2008.01.002, 2008.

Dauphin, Y., Ball, A. D., Castillo-Michel, H., Chevallard, C., Cuif, J.-P., Farre, B., Pouvreau, S., and Salomé, M.: In situ distribution and characterization of the organic content of the oyster shell Crassostrea gigas (Mollusca, Bivalvia), Micron, 44, 373–383, https://doi.org/10.1016/j.micron.2012.09.002, 2013.

De Yoreo, J. J., Gilbert, P. U. P. A., Sommerdijk, N. A. J. M., Penn, R. L., Whitelam, S., Joester, D., Zhang, H., Rimer, J. D., Navrotsky, A., Banfield, J. F., Wallace, A. F., Michel, F. M., Meldrum, F. C., Cölfen, H., and Dove, P. M.: Crystallization by particle attachment in synthetic, biogenic, and geologic environments, Science, 349, aaa6760, https://doi.org/10.1126/science.aaa6760, 2015.

Dellinger, M., West, A. J., Paris, G., Adkins, J. F., Pogge von Strandmann, P. A. E., Ullmann, C. V., Eagle, R. A., Freitas, P., Bagard, M.-L., Ries, J. B., Corsetti, F. A., Perez-Huerta, A., and Kampf, A. R.: The Li isotope composition of marine biogenic carbonates: Patterns and mechanisms, Geochimica et Cosmochimica Acta, 236, 315–335, https://doi.org/10.1016/j.gca.2018.03.014, 2018.

van Dijk, I., de Nooijer, L. J., Boer, W., and Reichart, G.-J.: Sulfur in foraminiferal calcite as a potential proxy for seawater carbonate ion concentration, Earth and Planetary Science Letters, 470, 64–72, https://doi.org/10.1016/j.epsl.2017.04.031, 2017.

van Dijk, I., Mouret, A., Cotte, M., Le Houedec, S., Oron, S., Reichart, G.-J., Reyes-Herrera, J., Filipsson, H. L., and Barras, C.: Chemical Heterogeneity of Mg, Mn, Na, S, and Sr in Benthic Foraminiferal Calcite, Frontiers in Earth Science, Volume 7-2019, 2019a.

van Dijk, I., Barras, C., de Nooijer, L. J., Mouret, A., Geerken, E., Oron, S., and Reichart, G.-J.: Coupled calcium and inorganic carbon uptake suggested by magnesium and sulfur incorporation in foraminiferal calcite, Biogeosciences, 16, 2115–2130, https://doi.org/10.5194/bg-16-2115-2019, 2019b.

Docampo, R. and Moreno, S. N. J.: Acidocalcisomes, Cell Calcium, 50, 113–119, https://doi.org/10.1016/j.ceca.2011.05.012, 2011.

Docampo, R., de Souza, W., Miranda, K., Rohloff, P., and Moreno, S. N. J.: Acidocalcisomes ? conserved from bacteria to man, Nature Reviews Microbiology, 3, 251–261, https://doi.org/10.1038/nrmicro1097, 2005.

Dubicka, Z., Bojanowski, M. J., Bijma, J., and Bickmeyer, U.: Mg-rich amorphous to Mg-low crystalline CaCO3 pathway in foraminifera, Heliyon, 9, https://doi.org/10.1016/j.heliyon.2023.e18331, 2023.

Dubicka, Z., Syczewski, M. D., Benning, L. G., Schreiber, A., Wirth, R., Witkowski, M., Bojanowski, M. J., Pałczyńska, A., Janse, M., and Bickmeyer, U.: Amorphous calcium carbonate loaded multilamellar vesicles within Amphistegina (Rotaliida) foraminifera, Acta Biomaterialia, 208, 525–537, https://doi.org/10.1016/j.actbio.2025.10.060, 2025.

Eggins, S. M., Sadekov, A., and De Deckker, P.: Modulation and daily banding of Mg/Ca in Orbulina universa tests by symbiont photosynthesis and respiration: a complication for seawater thermometry?, Earth and Planetary Science Letters, 225, 411–419, https://doi.org/10.1016/j.epsl.2004.06.019, 2004.

Erez, J.: The Source of Ions for Biomineralization in Foraminifera and Their Implications for Paleoceanographic Proxies, Reviews in Mineralogy and Geochemistry, 54, 115–149, https://doi.org/10.2113/0540115, 2003.

Evans, D., Webb, P. B., Penkman, K., Kröger, R., and Allison, N.: The Characteristics and Biological Relevance of Inorganic Amorphous Calcium Carbonate (ACC) Precipitated from Seawater, Crystal Growth & Design, 19, 4300–4313, https://doi.org/10.1021/acs.cgd.9b00003, 2019.

Evans, D., Gray, W. R., Rae, J. W. B., Greenop, R., Webb, P. B., Penkman, K., Kröger, R., and Allison, N.: Trace and major element incorporation into amorphous calcium carbonate (ACC) precipitated from seawater, Geochimica et Cosmochimica Acta, 290, 293–311, https://doi.org/10.1016/j.gca.2020.08.034, 2020.

Fakhraee, M., Crowe, S. A., and Katsev, S.: Sedimentary sulfur isotopes and Neoarchean ocean oxygenation, Sci Adv, 4, e1701835, https://doi.org/10.1126/sciadv.1701835, 2018.

Falini, G., Albeck, S., Weiner, S., and Addadi, L.: Control of Aragonite or Calcite Polymorphism by Mollusk Shell Macromolecules, Science, 271, 67–69, https://doi.org/10.1126/science.271.5245.67, 1996.

Falini, G., Fermani, S., and Goffredo, S.: Coral biomineralization: A focus on intra-skeletal organic matrix and calcification, Seminars in Cell & Developmental Biology, 46, 17–26, https://doi.org/10.1016/j.semcdb.2015.09.005, 2015.

Farquhar, J., Johnston, D. T., Wing, B. A., Habicht, K. S., Canfield, D. E., Airieau, S., and Thiemens, M. H.: Multiple sulphur isotopic interpretations of biosynthetic pathways: implications for biological signatures in the sulphur isotope record, Geobiology, 1, 27–36, https://doi.org/10.1046/j.1472-4669.2003.00007.x, 2003.

Fehrenbacher, J. S., Russell, A. D., Davis, C. V., Gagnon, A. C., Spero, H. J., Cliff, J. B., Zhu, Z., and Martin, P.: Link between light-triggered Mg-banding and chamber formation in the planktic foraminifera Neogloboquadrina dutertrei, Nature Communications, 8, 15441, https://doi.org/10.1038/ncomms15441, 2017.

Fernández-Díaz, L., Fernández-González, Á., and Prieto, M.: The role of sulfate groups in controlling CaCO3 polymorphism, Geochimica et Cosmochimica Acta, 74, 6064–6076, https://doi.org/10.1016/j.gca.2010.08.010, 2010.

Geerken, E., de Nooijer, L. J., Roepert, A., Polerecky, L., King, H. E., and Reichart, G. J.: Element banding and organic linings within chamber walls of two benthic foraminifera, Scientific Reports, 9, 3598, https://doi.org/10.1038/s41598-019-40298-y, 2019.

Gilbert, P. U. P. A., Bergmann, K. D., Boekelheide, N., Tambutté, S., Mass, T., Marin, F., Adkins, J. F., Erez, J., Gilbert, B., Knutson, V., Cantine, M., Hernández, J. O., and Knoll, A. H.: Biomineralization: Integrating mechanism and evolutionary history, Science Advances, 8, eabl9653, https://doi.org/10.1126/sciadv.abl9653, 2022.

Glock, N., Liebetrau, V., Vogts, A., and Eisenhauer, A.: Organic Heterogeneities in Foraminiferal Calcite Traced Through the Distribution of N, S, and I Measured With NanoSIMS: A New Challenge for Element-Ratio-Based Paleoproxies?, Frontiers in Earth Science, Volume 7-2019, 2019.

Glock, N., Richirt, J., Woehle, C., Algar, C., Armstrong, M., Eichner, D., Firrincieli, H., Makabe, A., Govindankutty Menon, A., Ishitani, Y., Hackl, T., Hubert-Huard, R., Kienast, M., Milker, Y., Mutzberg, A., Ni, S., Okada, S., Rakshit, S., Schmiedl, G., Steiner, Z., Tame, A., Zhang, Z., and Nomaki, H.: Widespread occurrence and relevance of phosphate storage in foraminifera, Nature, 638, 1000–1006, https://doi.org/10.1038/s41586-024-08431-8, 2025.

Goetschl, K. E., Purgstaller, B., Dietzel, M., and Mavromatis, V.: Effect of sulfate on magnesium incorporation in low-magnesium calcite, Geochimica et Cosmochimica Acta, 265, 505–519, https://doi.org/10.1016/j.gca.2019.07.024, 2019.

Gomes, M. L. and Hurtgen, M. T.: Sulfur isotope fractionation in modern euxinic systems: Implications for paleoenvironmental reconstructions of paired sulfate–sulfide isotope records, Geochimica et Cosmochimica Acta, 157, 39–55, https://doi.org/10.1016/j.gca.2015.02.031, 2015.

Gomes, M. L., Hurtgen, M. T., and Sageman, B. B.: Biogeochemical sulfur cycling during Cretaceous oceanic anoxic events: A comparison of OAE1a and OAE2, Paleoceanography, 31, 233–251, https://doi.org/10.1002/2015PA002869, 2016.

Goodenough, U., Heiss, A. A., Roth, R., Rusch, J., and Lee, J.-H.: Acidocalcisomes: Ultrastructure, Biogenesis, and Distribution in Microbial Eukaryotes, Protist, 170, 287–313, https://doi.org/10.1016/j.protis.2019.05.001, 2019.

Gussone, N., Langer, G., Thoms, S., Nehrke, G., Eisenhauer, A., Riebesell, U., and Wefer, G.: Cellular calcium pathways and isotope fractionation in Emiliania huxleyi, Geology, 34, 625–628, https://doi.org/10.1130/G22733.1, 2006.

Habicht, K. S., Gade, M., Thamdrup, B., Berg, P., and Canfield, D. E.: Calibration of Sulfate Levels in the Archean Ocean, Science, 298, 2372–2374, https://doi.org/10.1126/science.1078265, 2002.

He, M., Yu, X., Deng, W., Chen, X., Peng, X., Ta, K., Xu, H., Cui, Z., Yang, Q., Yang, Y., Zhang, Y., and Wei, G.: In Situ Analysis of Sulfur Isotopic Fractionation in Deep-Sea Corals Using Secondary-Ion Mass Spectrometry: Insights Into Vital Effects, Journal of Geophysical Research: Biogeosciences, 129, e2024JG008032, https://doi.org/10.1029/2024JG008032, 2024.

Helman, Y., Natale, F., Sherrell, R. M., LaVigne, M., Starovoytov, V., Gorbunov, M. Y., and Falkowski, P. G.: Extracellular matrix production and calcium carbonate precipitation by coral cells in vitro, Proceedings of the National Academy of Sciences, 105, 54–58, https://doi.org/10.1073/pnas.0710604105, 2008.

Hemleben, C., Be, A. W. H., Anderson, O. R., and Tuntivate, S.: Test morphology, organic layers and chamber formation of the planktonic foraminifer Globorotalia menardii (d'Orbigny), Journal of Foraminiferal Research, 7, 1–25, https://doi.org/10.2113/gsjfr.7.1.1, 1977.

Hemleben, C., Erson, O., Berthold, W., and Spindler, M.: Calcification and chamber formation in Foraminifera-a brief overview, Biomineralization in lower plants and animals (BSC Leadbeater, R Riding, eds) Clarendon Press, Oxford, 237–249, 1986.

Horita, J., Zimmermann, H., and Holland, H. D.: Chemical evolution of seawater during the Phanerozoic: Implications from the record of marine evaporites, Geochimica et Cosmochimica Acta, 66, 3733–3756, 2002.

House, W. A.: Inhibition of calcite crystal growth by inorganic phosphate, Journal of Colloid and Interface Science, 119, 505–511, https://doi.org/10.1016/0021-9797(87)90296-7, 1987.

House, W. A. and Donaldson, L.: Adsorption and coprecipitation of phosphate on calcite, Journal of Colloid and Interface Science, 112, 309–324, https://doi.org/10.1016/0021-9797(86)90101-3, 1986.

Jacob, D. E., Wirth, R., Agbaje, O. B. A., Branson, O., and Eggins, S. M.: Planktic foraminifera form their shells via metastable carbonate phases, Nature Communications, 8, 1265, https://doi.org/10.1038/s41467-017-00955-0, 2017.

Jauffrais, T., LeKieffre, C., Schweizer, M., Geslin, E., Metzger, E., Bernhard, J. M., Jesus, B., Filipsson, H. L., Maire, O., and Meibom, A.: Kleptoplastidic benthic foraminifera from aphotic habitats: insights into assimilation of inorganic C, N and S studied with sub-cellular resolution, Environmental Microbiology, 21, 125–141, https://doi.org/10.1111/1462-2920.14433, 2019.

Jørgensen, B. B., Erez, J., Revsbech, P., and Cohen, Y.: Symbiotic photosynthesis in a planktonic foraminiferan, Globigerinoides sacculifer (Brady), studied with microelectrodes, Limnology and Oceanography, 30, 1253–1267, https://doi.org/10.4319/lo.1985.30.6.1253, 1985.

Kah, L. C., Lyons, T. W., and Frank, T. D.: Low marine sulphate and protracted oxygenation of the Proterozoic biosphere, Nature, 431, 834–838, https://doi.org/http://www.nature.com/nature/journal/v431/n7010/suppinfo/nature02974_S1.html, 2004.

Kahil, K., Weiner, S., Addadi, L., and Gal, A.: Ion Pathways in Biomineralization: Perspectives on Uptake, Transport, and Deposition of Calcium, Carbonate, and Phosphate, J. Am. Chem. Soc., 143, 21100–21112, https://doi.org/10.1021/jacs.1c09174, 2021.

Kampschulte, A., Bruckschen, P., and Strauss, H.: The sulphur isotopic composition of trace sulphates in Carboniferous brachiopods: implications for coeval seawater, correlation with other geochemical cycles and isotope stratigraphy, Chemical Geology, 175, 149–173, https://doi.org/10.1016/S0009-2541(00)00367-3, 2001.

Kitano, Y., Okumura, M., and Idogaki, M.: Incorporation of sodium, chloride and sulfate with calcium carbonate, Geochem. J, 9, 75–84, 1975.

Kontrec, J., Kralj, D., Brečević, L., Falini, G., Fermani, S., Noethig-Laslo, V., and Mirosavljević, K.: Incorporation of Inorganic Anions in Calcite, Eur. J. Inorg. Chem., 2004, 4579–4585, https://doi.org/10.1002/ejic.200400268, 2004.

Kopp, C., Domart-Coulon, I., Escrig, S., Humbel, B. M., Hignette, M., and Meibom, A.: Subcellular Investigation of Photosynthesis-Driven Carbon Assimilation in the Symbiotic Reef Coral Pocillopora damicornis, mBio, 6, 10.1128/mbio.02299-14, https://doi.org/10.1128/mbio.02299-14, 2015.

ten Kuile, B. and Erez, J.: Uptake of inorganic carbon and internal carbon cycling in symbiont-bearing benthonic foraminifera, Marine Biology, 94, 499–509, https://doi.org/10.1007/BF00431396, 1987.

ter Kuile, B. and Erez, J.: The size and function of the internal inorganic carbon pool of the foraminifer Amphistegina lobifera, Marine Biology, 99, 481–487, https://doi.org/10.1007/BF00392555, 1988.

Kunioka, D., Shirai, K., Takahata, N., Sano, Y., Toyofuku, T., and Ujiie, Y.: Microdistribution of Mg/Ca, Sr/Ca, and Ba/Ca ratios in Pulleniatina obliquiloculata test by using a NanoSIMS: Implication for the vital effect mechanism, Geochemistry, Geophysics, Geosystems, 7, https://doi.org/10.1029/2006GC001280, 2006.

LaFlamme, C., Barré, G., Fiorentini, M. L., Beaudoin, G., Occhipinti, S., and Bell, J.: A significant seawater sulfate reservoir at 2.0 Ga determined from multiple sulfur isotope analyses of the Paleoproterozoic Degrussa Cu-Au volcanogenic massive sulfide deposit, Western Australia, Geochimica et Cosmochimica Acta, 295, 178–193, https://doi.org/10.1016/j.gca.2020.12.018, 2021.

Langer, G., Gussone, N., Nehrke, G., Riebesell, U., Eisenhauer, A., Kuhnert, H., Rost, B., Trimborn, S., and Thoms, S.: Coccolith strontium to calcium ratios in Emiliania huxleyi: The dependence on seawater strontium and calcium concentrations, Limnology and Oceanography, 51, 310–320, https://doi.org/10.4319/lo.2006.51.1.0310, 2006.

Langer, G., Nehrke, G., Thoms, S., and Stoll, H.: Barium partitioning in coccoliths of Emiliania huxleyi, Geochimica et Cosmochimica Acta, 73, 2899–2906, https://doi.org/10.1016/j.gca.2009.02.025, 2009.

Langer, M. R.: Biosynthesis of glycosaminoglycans in foraminifera: A review, Marine Micropaleontology, 19, 245–255, https://doi.org/10.1016/0377-8398(92)90031-E, 1992.

LeKieffre, C., Bernhard, J. M., Mabilleau, G., Filipsson, H. L., Meibom, A., and Geslin, E.: An overview of cellular ultrastructure in benthic foraminifera: New observations of rotalid species in the context of existing literature, Marine Micropaleontology, 138, 12–32, https://doi.org/10.1016/j.marmicro.2017.10.005, 2018.

LeKieffre, C., Jauffrais, T., Bernhard, J. M., Filipsson, H. L., Schmidt, C., Roberge, H., Maire, O., Panieri, G., Geslin, E., and Meibom, A.: Ammonium and Sulfate Assimilation Is Widespread in Benthic Foraminifera, Frontiers in Marine Science, Volume 9-2022, 2022.

Lemelle, L., Bartolini, A., Simionovici, A., Tucoulou, R., De Nolf, W., Bassinot, F., and de Garidel-Thoron, T.: Nanoscale trace metal imprinting of biocalcification of planktic foraminifers by Toba's super-eruption, Scientific Reports, 10, 10974, https://doi.org/10.1038/s41598-020-67481-w, 2020.

Lin, Y.-P. and Singer, P. C.: Inhibition of calcite precipitation by orthophosphate: Speciation and thermodynamic considerations, Geochimica et Cosmochimica Acta, 70, 2530–2539, https://doi.org/10.1016/j.gca.2006.03.002, 2006.

Lorens, R. B. and Bender, M. L.: The impact of solution chemistry on Mytilus edulis calcite and aragonite, Geochimica et Cosmochimica Acta, 44, 1265–1278, https://doi.org/10.1016/0016-7037(80)90087-3, 1980.

Mavromatis, V., Gautier, Q., Bosc, O., and Schott, J.: Kinetics of Mg partition and Mg stable isotope fractionation during its incorporation in calcite, Geochimica et Cosmochimica Acta, 114, 188–203, https://doi.org/10.1016/j.gca.2013.03.024, 2013.

Mucci, A.: Influence of temperature on the composition of magnesian calcite overgrowths precipitated from seawater, Geochimica et Cosmochimica Acta, 51, 1977–1984, https://doi.org/10.1016/0016-7037(87)90186-4, 1987.

Nehrke, G., Keul, N., Langer, G., De Nooijer, L., Bijma, J., and Meibom, A.: A new model for biomineralization and trace-element signatures of Foraminifera tests, Biogeosciences, 10, 6759–6767, 2013.

Nomaki, H., Bernhard, J. M., Ishida, A., Tsuchiya, M., Uematsu, K., Tame, A., Kitahashi, T., Takahata, N., Sano, Y., and Toyofuku, T.: Intracellular Isotope Localization in Ammonia sp. (Foraminifera) of Oxygen-Depleted Environments: Results of Nitrate and Sulfate Labeling Experiments, Frontiers in Microbiology, Volume 7-2016, 2016.

de Nooijer, L. J., Langer, G., Nehrke, G., and Bijma, J.: Physiological controls on seawater uptake and calcification in the benthic foraminifer Ammonia tepida, Biogeosciences, 6, 2669–2675, 2009.

de Nooijer, L. J., Spero, H. J., Erez, J., Bijma, J., and Reichart, G. J.: Biomineralization in perforate foraminifera, Earth-Science Reviews, 135, 48–58, https://doi.org/10.1016/j.earscirev.2014.03.013, 2014.

Oae, S.: Organic chemistry of sulfur, Springer Science & Business Media, 2012.

Ohkouchi, N., Kawamura, K., Kajiwara, Y., Wada, E., Okada, M., Kanamatsu, T., and Taira, A.: Sulfur isotope records around Livello Bonarelli (northern Apennines, Italy) black shale at the Cenomanian-Turonian boundary, Geology, 27, 535, 1999.

Osburn, M. R., Owens, J., Bergmann, K. D., Lyons, T. W., and Grotzinger, J. P.: Dynamic changes in sulfate sulfur isotopes preceding the Ediacaran Shuram Excursion, Geochimica et Cosmochimica Acta, 170, 204–224, https://doi.org/10.1016/j.gca.2015.07.039, 2015.

Paris, G., Sessions, A. L., Subhas, A. V., and Adkins, J. F.: MC-ICP-MS measurement of δ34S and Δ33S in small amounts of dissolved sulfate, Chemical Geology, 345, 50–61, https://doi.org/10.1016/j.chemgeo.2013.02.022, 2013.

Paris, G., Fehrenbacher, J. S., Sessions, A. L., Spero, H. J., and Adkins, J. F.: Experimental determination of carbonate-associated sulfate δ34S in planktonic foraminifera shells, Geochemistry, Geophysics, Geosystems, 15, 1452–1461, https://doi.org/10.1002/2014gc005295, 2014a.

Paris, G., Adkins, J. F., Sessions, A. L., Webb, S. M., and Fischer, W. W.: Neoarchean carbonate–associated sulfate records positive Δ33S anomalies, Science, 346, 739–741, https://doi.org/10.1126/science.1258211, 2014b.

Paris, G., Fischer, W. W., Johnson, J. E., Webb, S. M., Present, T. M., Sessions, A. L., and Adkins, J. F.: Deposition of sulfate aerosols with positive Δ33S in the Neoarchean, Geochimica et Cosmochimica Acta, 285, 1–20, https://doi.org/10.1016/j.gca.2020.06.028, 2020.

Patron, N. J., Durnford, D. G., and Kopriva, S.: Sulfate assimilation in eukaryotes: fusions, relocations and lateral transfers, BMC Evolutionary Biology, 8, 39, https://doi.org/10.1186/1471-2148-8-39, 2008.

Paytan, A., Kastner, M., Campbell, D., and Thiemens, M. H.: Sulfur Isotopic Composition of Cenozoic Seawater Sulfate, Science, 282, 1459–1462, https://doi.org/10.1126/science.282.5393.1459, 1998.

Piłsyk, S. and Paszewski, A.: Sulfate permeasesphylogenetic diversity of sulfate transport., Acta Biochimica Polonica, 56, 2009.

Plant, L. J. and House, W. A.: Precipitation of calcite in the presence of inorganic phosphate, Colloids and Surfaces A: Physicochemical and Engineering Aspects, 203, 143–153, https://doi.org/10.1016/S0927-7757(01)01089-5, 2002.

Present, T. M., Paris, G., Burke, A., Fischer, W. W., and Adkins, J. F.: Large Carbonate Associated Sulfate isotopic variability between brachiopods, micrite, and other sedimentary components in Late Ordovician strata, Earth and Planetary Science Letters, 432, 187–198, https://doi.org/10.1016/j.epsl.2015.10.005, 2015.

Present, T. M., Adkins, J. F., and Fischer, W. W.: Variability in Sulfur Isotope Records of Phanerozoic Seawater Sulfate, Geophysical Research Letters, 47, e2020GL088766, https://doi.org/10.1029/2020GL088766, 2020.

Raz, S., Weiner, S., and Addadi, L.: Formation of High-Magnesian Calcites via an Amorphous Precursor Phase: Possible Biological Implications, Advanced Materials, 12, 38–42, https://doi.org/10.1002/(SICI)1521-4095(200001)12:1%3C38::AID-ADMA38%3E3.0.CO;2-I, 2000.

Rees, C. E., Jenkins, W. J., and Monster, J.: The sulphur isotopic composition of ocean water sulphate, Geochimica et Cosmochimica Acta, 42, 377–381, https://doi.org/10.1016/0016-7037(78)90268-5, 1978.

Ren, C., Li, Y., Zhou, Q., and Li, W.: Phosphate uptake by calcite: Constraints of concentration and pH on the formation of calcium phosphate precipitates, Chemical Geology, 579, 120365, https://doi.org/10.1016/j.chemgeo.2021.120365, 2021.

Rennie, V. C. F., Paris, G., Sessions, A. L., Abramovich, S., Turchyn, A. V., and Adkins, J. F.: Cenozoic record of δ34S in foraminiferal calcite implies an early Eocene shift to deep-ocean sulfide burial, Nature Geoscience, https://doi.org/10.1038/s41561-018-0200-y, 2018.

Richardson, J. A., Newville, M., Lanzirotti, A., Webb, S. M., Rose, C. V., Catalano, J. G., and Fike, D. A.: Depositional and diagenetic constraints on the abundance and spatial variability of carbonate-associated sulfate, Chemical Geology, 523, 59–72, https://doi.org/10.1016/j.chemgeo.2019.05.036, 2019a.

Richardson, J. A., Newville, M., Lanzirotti, A., Webb, S. M., Rose, C. V., Catalano, J. G., and Fike, D. A.: The source of sulfate in brachiopod calcite: Insights from µ-XRF imaging and XANES spectroscopy, Chemical Geology, 529, 119328, https://doi.org/10.1016/j.chemgeo.2019.119328, 2019b.

Richardson, J. A., Lepland, A., Hints, O., Prave, A. R., Gilhooly, W. P., Bradley, A. S., and Fike, D. A.: Effects of early marine diagenesis and site-specific depositional controls on carbonate-associated sulfate: Insights from paired S and O isotopic analyses, Chemical Geology, 584, 120525, https://doi.org/10.1016/j.chemgeo.2021.120525, 2021.

Rodriguez-Blanco, J. D., Shaw, S., Bots, P., Roncal-Herrero, T., and Benning, L. G.: The role of pH and Mg on the stability and crystallization of amorphous calcium carbonate, Journal of Alloys and Compounds, 536, S477–S479, https://doi.org/10.1016/j.jallcom.2011.11.057, 2012.

Rollion-Bard, C. and Erez, J.: Intra-shell boron isotope ratios in benthic foraminifera: Implications for paleo-pH reconstructions, Geochimica et Cosmochimica Acta, 74, 1530–1536, 2010.

Saulnier, S., Rollion-Bard, C., Vigier, N., and Chaussidon, M.: Mg isotope fractionation during calcite precipitation: An experimental study, Geochimica et Cosmochimica Acta, 91, 75–91, https://doi.org/10.1016/j.gca.2012.05.024, 2012.

Schiff, J. A.: Pathways of Assimilatory Sulphate Reduction in Plants and Microorganisms, in: Ciba Foundation Symposium 72 - Sulphur in Biology, 49–69, https://doi.org/10.1002/9780470720554.ch4, 1980.

Sim, M. S., Woo, D. K., Kim, B., Jeong, H., Joo, Y. J., Hong, Y. W., and Choi, J. Y.: What Controls the Sulfur Isotope Fractionation during Dissimilatory Sulfate Reduction?, ACS Environ. Au, 3, 76–86, https://doi.org/10.1021/acsenvironau.2c00059, 2023.

Spero, H. J.: Life history and stable isotope geochemistry of planktonic foraminifera, The Paleontological Society Papers, 4, 7–36, 1998.

Spero, H. J., Eggins, S. M., Russell, A. D., Vetter, L., Kilburn, M. R., and Hönisch, B.: Timing and mechanism for intratest Mg/Ca variability in a living planktic foraminifer, Earth and Planetary Science Letters, 409, 32–42, https://doi.org/10.1016/j.epsl.2014.10.030, 2015a.

Spero, H. J., Eggins, S. M., Russell, A. D., Vetter, L., Kilburn, M. R., and Hönisch, B.: Timing and mechanism for intratest Mg/Ca variability in a living planktic foraminifer, Earth and Planetary Science Letters, 409, 32–42, https://doi.org/10.1016/j.epsl.2014.10.030, 2015b.

Tambutté, S., Tambutté, E., Zoccola, D., and Allemand, D.: Organic Matrix and Biomineralization of Scleractinian Corals, in: Handbook of Biomineralization, 243–259, https://doi.org/10.1002/9783527619443.ch14, 2007.

Tanaka, K., Okaniwa, N., Miyaji, T., Murakami-Sugihara, N., Zhao, L., Tanabe, K., Schöne, B. R., and Shirai, K.: Microscale magnesium distribution in shell of the Mediterranean mussel Mytilus galloprovincialis: An example of multiple factors controlling Mg/Ca in biogenic calcite, Chemical Geology, 511, 521–532, https://doi.org/10.1016/j.chemgeo.2018.10.025, 2019.

Thaler, C., Paris, G., Dellinger, M., Dissard, D., Berland, S., Marie, A., Labat, A., and Bartolini, A.: Impact of seawater sulfate concentration on sulfur concentration and isotopic composition in calcite of two cultured benthic foraminifera, EGUsphere, 2023, 1–29, 2023.

The Cenozoic CO2 Proxy Integration Project (CenCO2PIP) Consortium, Hönisch, B., Royer, D. L., Breecker, D. O., Polissar, P. J., Bowen, G. J., Henehan, M. J., Cui, Y., Steinthorsdottir, M., McElwain, J. C., Kohn, M. J., Pearson, A., Phelps, S. R., Uno, K. T., Ridgwell, A., Anagnostou, E., Austermann, J., Badger, M. P. S., Barclay, R. S., Bijl, P. K., Chalk, T. B., Scotese, C. R., de la Vega, E., DeConto, R. M., Dyez, K. A., Ferrini, V., Franks, P. J., Giulivi, C. F., Gutjahr, M., Harper, D. T., Haynes, L. L., Huber, M., Snell, K. E., Keisling, B. A., Konrad, W., Lowenstein, T. K., Malinverno, A., Guillermic, M., Mejía, L. M., Milligan, J. N., Morton, J. J., Nordt, L., Whiteford, R., Roth-Nebelsick, A., Rugenstein, J. K. C., Schaller, M. F., Sheldon, N. D., Sosdian, S., Wilkes, E. B., Witkowski, C. R., Zhang, Y. G., Anderson, L., Beerling, D. J., Bolton, C., Cerling, T. E., Cotton, J. M., Da, J., Ekart, D. D., Foster, G. L., Greenwood, D. R., Hyland, E. G., Jagniecki, E. A., Jasper, J. P., Kowalczyk, J. B., Kunzmann, L., Kürschner, W. M., Lawrence, C. E., Lear, C. H., Martínez-Botí, M. A., Maxbauer, D. P., Montagna, P., Naafs, B. D. A., Rae, J. W. B., Raitzsch, M., Retallack, G. J., Ring, S. J., Seki, O., Sepúlveda, J., Sinha, A., Tesfamichael, T. F., Tripati, A., van der Burgh, J., Yu, J., Zachos, J. C., and Zhang, L.: Toward a Cenozoic history of atmospheric CO2, Science, 382, eadi5177, https://doi.org/10.1126/science.adi5177, 2023.

Timofeeff, M. N., Lowenstein, T. K., Brennan, S. T., Demicco, R. V., Zimmermann, H., Horita, J., and Von Borstel, L. E.: Evaluating seawater chemistry from fluid inclusions in halite: examples from modern marine and nonmarine environments, Geochimica et Cosmochimica Acta, 65, 2293–2300, 2001.

Tostevin, R., Turchyn, A. V., Farquhar, J., Johnston, D. T., Eldridge, D. L., Bishop, J. K. B., and McIlvin, M.: Multiple sulfur isotope constraints on the modern sulfur cycle, Earth and Planetary Science Letters, 396, 14–21, https://doi.org/10.1016/j.epsl.2014.03.057, 2014.

Tyszka, J., Godos, K., Goleń, J., and Radmacher, W.: Foraminiferal organic linings: Functional and phylogenetic challenges, Earth-Science Reviews, 220, 103726, https://doi.org/10.1016/j.earscirev.2021.103726, 2021.

Weiner, S. and Addadi, L.: Crystallization pathways in biomineralization, Annual review of materials research, 41, 21–40, 2011.

Weiner, S. and Erez, J.: Organic matrix of the shell of the foraminifer, Heterostegina depressa, The Journal of Foraminiferal Research, 14, 206–212, https://doi.org/10.2113/gsjfr.14.3.206, 1984.

Weiner, S., Levi-Kalisman, Y., Raz, S., and Addadi, L.: Biologically Formed Amorphous Calcium Carbonate, Connective Tissue Research, 44, 214–218, https://doi.org/10.1080/03008200390181681, 2003.

Zou, Z., Xie, J., Macías-Sánchez, E., and Fu, Z.: Nonclassical Crystallization of Amorphous Calcium Carbonate in the Presence of Phosphate Ions, Crystal Growth & Design, 21, 414–423, https://doi.org/10.1021/acs.cgd.0c01245, 2021.